Ore Geology Reviews 125 (2020) 103665

Contents lists available at ScienceDirect

Ore Geology Reviews

journal homepage: www.elsevier.com/locate/oregeorev

Contribution to the origin of Mn-U-Be-HREE-enrichment in phosphorite, near Bükkszentkereszt, NE Hungary

Péter Gál[a], Márta Polgári[b,c,*], Sándor Józsa[a], Ildikó Gyollai[b], Ivett Kovács[b], Máté Szabó[b], Krisztián Fintor[d]

[a] Eötvös Loránd University, Dept. Petrology and Geochemistry, 1117 Budapest, Pázmány P. sétány 1/c, Hungary
[b] Research Centre for Astronomy and Geosciences, Institute for Geological and Geochemical Research, 1112 Budapest, Budaörsi út 45, Hungary
[c] Eszterházy Károly University, Dept. of Natural Geography and Geoinformatics, 3300 Eger, Leányka utca 6/C, Hungary
[d] Szeged University, Dept. of Mineralogy, Geochemistry and Petrology, 6722 Szeged, Egyetem utca 2-6, Hungary

ARTICLE INFO

Keywords:
Beryllium
Hydrothermal
Microbial
Phosphorite
Raman spectroscopy
Uranium

ABSTRACT

Strongly deformed phosphorite layers enriched with U-Be-Mn-REE occur in a weathered Triassic metarhyolite tuff near the town of Bükkszentkereszt, NE Hungary. The phosphorite is massive or earthy, has an especially fine-grained texture, and forms inhomogeneous bands with different Mn-oxide contents.

High-resolution optical rock microscopy investigations helped to distinguish mineralized biosignatures, filamentous, vermiform structures, and coccoid-like aggregates. These microstructures encompass almost the whole phosphorite. Based on *in situ* FTIR and Raman spectroscopy, the phosphorites contain ferrihydrite and pyrite, and also different types of embedded organic matter. These structures can be interpreted as series of Fe-rich biomats, forming microbialites. On a larger scale, these microstructures can play a role in shaping the stratiform structure by evolving stromatolite-like bands.

Results presented here propose a new interpretation of the origin of the P-Mn-U-Be-HREE-enrichment. The Bükkszentkereszt occurrence claim a mineralized microbially mediated deposit, and our results support this scenario based on the mineralized microbial structures, the embedded minerals, and the presence of organic matter.

1. Introduction

Phosphorite is a marine sedimentary rock type containing at least 18 wt% P_2O_5 and is the main ore of the element phosphorous (Pufahl and Groat, 2017). Phosphorous is an essential nutrient for animals and plants, so primarily it is an agricultural resource. The formation of economically important phosphorite deposits requires special depositional and diagenetic conditions (Kolodny and Luz, 1992). The formation of phosphorite was temporally connected to specific phosphogenic epochs and spatially to phosphogenic provinces (Cook and McElhinny, 1979). Phosphates are the main ore-forming minerals of phosphorous, particularly apatite (commonly in the form of francolite – carbonate-rich fluorapatite, general formula: $Ca_{lo-a-b}Na_aMg_b(PO_4)_{6-x}(CO_3)_{x-y-z}(CO_3{\cdot}F)_y(SO_4)F_2$). The lattice structure of this mineral is conducive to various major and trace element substitutions (Jarvis, 1995). Due to its tendency to contain substituting trace elements, phosphate rock is on the list of critical raw materials all over the world. Phosphorite deposits can be the source of U and REE elements (typically 50–200 ppm U content and 500–2000 ppm REE), so phosphorite is also a significant high-tech resource (Pufahl and Groat, 2017).

A uranium research program took place between 1969 and 1973 near Bükkszentkereszt, in the Bükk Mts., NE Hungary (Fig. 1). A positive U-anomaly was detected by ground gamma-ray surveys in a small outcrop of weathered pyroclastics of the Triassic, Bagolyhegy Metarhyolite Formation (Szabó and Vincze, 2013; Németh et al., 2015). The source of the anomaly was identified as strongly deformed, dark coloured, Mn-oxide rich, clayey layers of 100–300 mm thick and containing small phosphorite lenses. Later, drill exploration found thin, irregular run-out lenses at shallow depth. The indication was not mined, because its known parameters did not reach an economically viable level (Csáki and Csáki, 1973; Szabó and Vincze, 2013) (Fig. 2).

Earlier investigations supposed that hydrothermal fluids discharging in the cataclastic crack zones of the metarhyolite tuff generated the phosphorite. These fluids could be the result of the heat effect of the

* Corresponding author at: Research Centre for Astronomy and Geosciences, Institute for Geological and Geochemical Research, 1112 Budapest, Budaörsi út 45, Hungary.
E-mail addresses: rodokrozit@gmail.com (M. Polgári), sandor-jozsa@caesar.elte.hu (S. Józsa).

https://doi.org/10.1016/j.oregeorev.2020.103665
Received 14 April 2020; Received in revised form 24 June 2020; Accepted 29 June 2020
Available online 04 July 2020

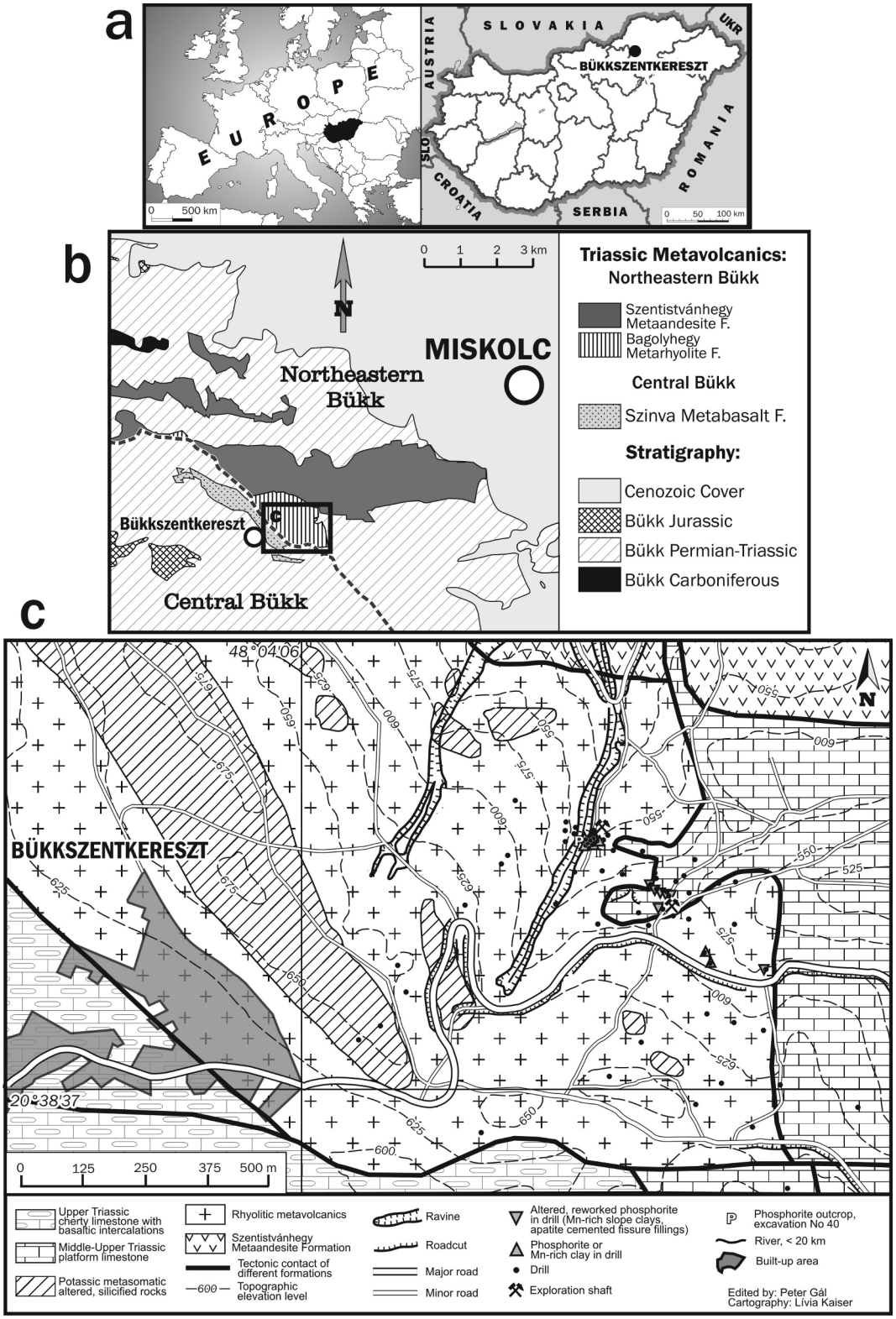

Fig. 1. The location of Bükkszentkereszt deposit (a-b); (c) Geological sketch map of the area (cartoon by PG). GPS location of Bükkszentkereszt: N 48^0 04′ 06″, E 20^0 38′ 37″.

Alpine regional epimetamorphism and/or submarine exhalations (Csáki and Csáki, 1973; Kubovics et al., 1989; Szabó and Vincze, 2013). However, recent investigations propose a syngenetic origin, in connection with submarine hot spring exhalations (Németh pers. comm. 2017).

New, complex investigations were performed on 10 samples in the Department of Petrology and Geochemistry, Eötvös University, and in the Institute for Geological and Geochemical Research, Research Centre for Astronomy and Earth Sciences, Budapest. Preliminary observations on thin sections showed thin, Mn-oxide and Fe-oxide-hydroxide bands

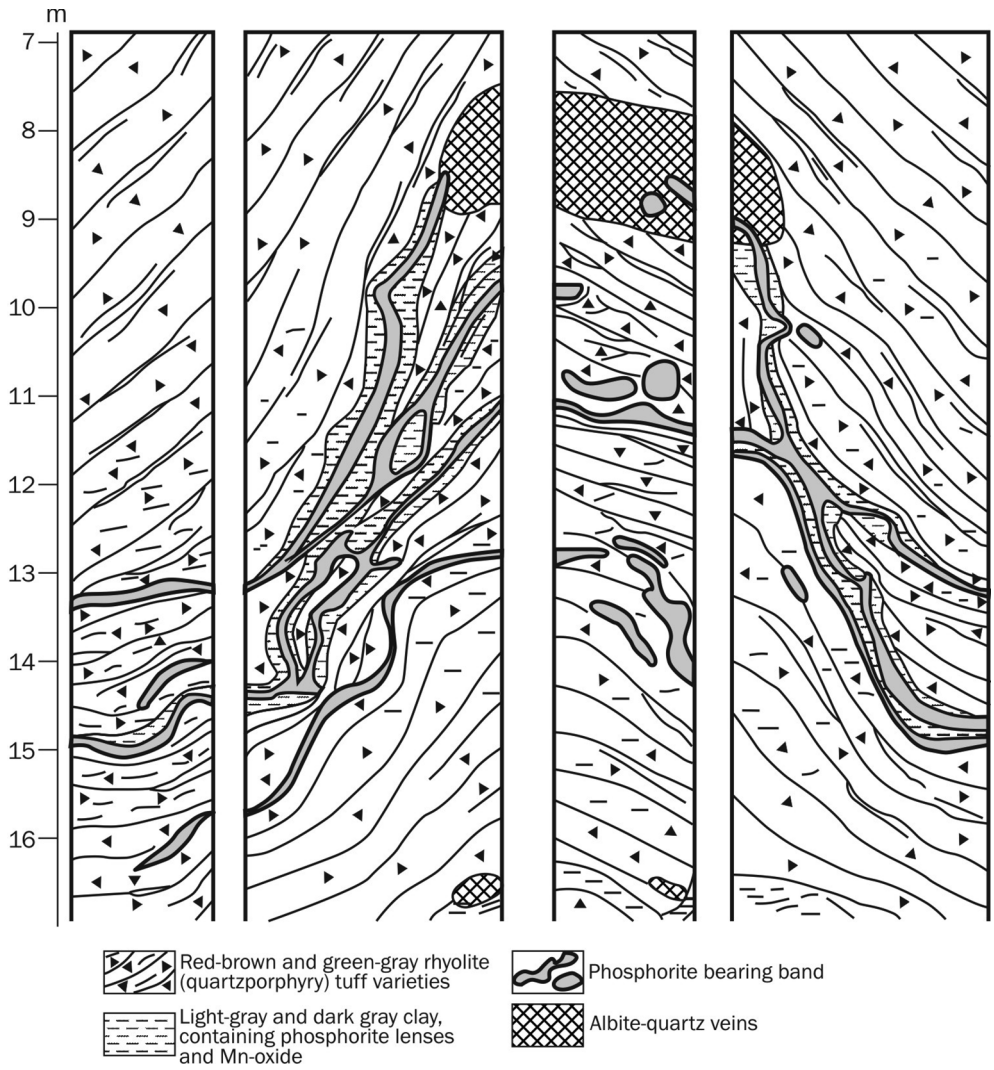

Fig. 2. Section of the ore mineralized system in Shaft No. II (modified after Szabó & Vincze 2013).

including stromatolite-like, filamentous and coccoid-like microstructures. According to the hypothesis of Polgári (2016), the Bükkszentkereszt occurrence is a mineralized microbially mediated deposit based on textural evidence and enrichment of bioessential elements (P, Mn, U, Be, As, Zn). Recent analogies and experiments prove that microbial colonies reflect metabolic processes which are accompanied by the enrichment of some elements. The complex activity of the colonies was capable of creating ore deposits over geological time-scales (Polgári et al., 2012a, 2012b, 2019; Knoll et al., 2012; Yu et al., 2019; Biondi et al., 2020).

The aim of this study is to find evidence for mineralized biosignatures, investigate the presence of organic compounds, and clarify the role of microbial mediation in forming the phosphorite layers and lenses through using complex investigation methods and structural hierarchical interpretation.

2. Geological setting and characterisation of the phosphorite

2.1. Geological setting

The Bükk Mountains are located in NE Hungary (Fig. 1). This is a less than 1000 m high mountain range which raised from the basement of the Neogene-Quarter Pannonian Basin as an island-like block built up mostly from a Paleozoic to Mesozoic series of sedimentary-volcanic rocks (Less et al., 2005; Haas et al., 2014). Tectonically, the Bükk Mts. belong to the Bükk Unit, which occurs at the eastern part of the Mid-Hungarian Main Unit (MH MU). The MH MU is a shearing zone of microplates that broke apart and consolidated from Dinaridic and S-Alpine Units and were transported a few hundred kilometers to the Northeast (Kovács and Haas, 2010; Haas et al., 2014). The Bükk Unit has a nappe structure; most of its surficial part consists of discontinuous sequences of the Bükk *para*-autochtonous formed between the Carboniferous and Jurassic and its sequence shows strong similarities to some units of the Dinarides (Jadar-block, Sana-Una; Pešic et al., 1988; Filipović et al., 2003; Kovács and Haas, 2010; Haas et al., 2014). In the Triassic sequence of the Bükk Paraautochtonous, volcanic rocks occur in several horizons. A significant, mostly NW-SE striking strike-slip fault cuts the Mesozoic sequence (Less et al., 2005). North of the fault, among Anisian and Ladinian platform carbonates, calc-alkaline acidic-intermediate volcanic rocks occur that belong to the ca. 240 Ma old Szentistvánhegy Metaandesite Formation (SMF; Less et al., 2005; Gál et al., 2018). South of the fault, a small amount of SMF and alkaline basaltic intercalations occur in Carnian deep marine carbonates (Szoldán, 1990). Along the fault near Bükkszentkereszt, possibly in fault slice position with uncertain Lower Triassic age, a small (2 km^2), calc-alkaline, acidic volcanic body occurs called the Bagolyhegy Metarhyolite Formation (BMF). Its petrography and geochemistry are very similar to metasomatized Permian rhyolites of the Tisia Megaunit in southern Hungary, but Permian volcanics are not known to occur in the Bükk Unit (Gál et al., 2018). The volcanic-sedimentary sequence of the

Bükk unit suffered regional anchizonal Alpine metamorphism in the Cretaceous, manifested by the illite crystallinity index and metamorphic mineral assemblages characteristic for 2.5–3 kbar and T_{max} around 350 °C, with a 6–14 km thick layer load (Árkai, 1983). Árkai et al. (1995) calculated 80 Ma K/Ar ages for cooling to 260 ± 20 °C.

The stratigraphic position of the BMF, the host rock of the phosphorite, is not clear yet; it occurs between the SMF and Carnian cherty limestones and metabasalts (Less et al., 2005; Gál et al., 2018). Geochemically, the BMF has rhyolitic composition. Post-magmatic metasomatic and metamorphic processes strongly altered the main element composition, so their exact petrological classification is uncertain (Less et al., 2005; Zajzon et al., 2014). The metamorphism caused sericitic and/or chloritic alteration and modified the original volcanic texture (structure) of rocks; mainly crumbly, thin laminated sericite shale occurs (Less et al., 2005). Most of the rhyolitic rocks have a pyroclastic origin, as interpreted from their textural features. They contain small amounts of quartz-feldspar phenocrysts (quartz is usually broken into shards) and also strongly deformed-elongated-silicified pumice- and lithic clasts of up to a few cm in size.

2.2. Occurrence, mineralogy and geochemistry of the phosphorite

During the uranium ore exploration between 1969 and 1973 dozens of shallow and some deep drillings with cores, furthermore two exploration shafts and several trenches were made. Anomalies were found only at the southeast, strongly tectonized edge of the metarhyolite formation along a cca. 470 m long and maximum 65 m wide zone. The ore bearing sections are discontinuous because of the tectonic fragmentation, the biggest with a cca. 50 × 25 m areal extension was found in 10–20 m depth, in which the phosphorite body reached 0,5–2 m thickness, but in its outer part only a few tens of cm thick manganiferous clay was found. The phosphorite body means irregular repetition of 5–20 cm thick irregular run out massive apatite rich lenses and rolls in earthy, manganiferous clay matrix. In a deep valley side this body had a natural outcrop which was excavated well. In some section of the anomalous zone totally weathered and reworked P-U-rich material was found in form of manganiferous clay layers with massive Mn-oxide concretions within young slope clays and U-bearing apatite crack fillings (Csáki and Csáki, 1973; Szabó and Vincze, 2013).

The phosphorite lenses have a laminated structure, in the form of inhomogeneous, light cream, dark brownish coloured thin bands whose material is especially fine-grained. Within or in connection with the phosphorite, different massive Mn-oxide lenses occur. The phosphorite lenses have micro-brecciated margins containing fragments of the host rock and coarse-grained massy quartz, cemented by apatite and Mn-oxide (Csáki and Csáki, 1973; Szabó and Vincze, 2013). In the lighter and also harder bands quartz, albite and a small amount of apatite occur, while in the brown bands the main component is apatite; their different colours depend on their respective Mn-oxide content. Rare earthy yellow bands are smectite-rich (Zajzon et al., 2014).

Based on SEM-EDX analyses, the apatite is mostly fluorapatite (Kubovics et al., 1989; Zajzon et al., 2014), but DTG and FTIR analyses also detected hydroxyapatite and carbonate-apatite (Szabó and Vincze, 2013). According to XRD analyses, variable Mn-oxide minerals occur (partly secondary): pyrolusite, cryptomelane, todorokite, ramsdellite, manganomelane, lithiophorite and probably bermanite and withoreite, with the first three being the main components (Szabó and Vincze, 2013; Zajzon et al., 2014). Numerous phyllosilicates also occur up to a few wt. %: 10 Å mica, hydrated halloysite, 15 Å smectite and sericite-muscovite type ordered mica (Polgári et al., 2000; Zajzon et al., 2014). SEM-EDX analyses determined mica as fluorophlogopite, smectite as nontronite and Ca-rich saponite.

Accessory minerals of the phosphorites determined by XRD analysis are the following: calcite, K-feldspar, goethite, dufrénite, amorphous material (most probably Mn oxide and/or Fe oxide-hydroxide). Uraninite, beryllonite, and bertrandite were also detected as uncertain traces (Selmeczi and Antal, 1974; Kubovics et al., 1989; Szabó and Vincze, 2013; Zajzon et al., 2014). DTG analyses detected also traces of opal, zeolite, rhodochrosite, pyrite, magnetite, and 0.2–0.6 wt% of organic material (Selmeczi and Antal, 1974; Kubovics et al., 1989). Analyses on heavy mineral separatum elaborated by electromagnetic processes found a negligible quantity of uncertainly determined uranophane, uraninite, vernadite, tourmaline, barite, and beryllonite (Szabó and Vincze, 2013).

The apatite is cryptocrystalline and often forms a needle-like spherulitic texture. In the inner part of the spherulites star-like forms built up, opaque laminae can often be seen. Micro-fissures are covered by columnar, idiomorphic or needle-like apatite crystals. The massy apatite often has microporosity, in which walls are composed of crystallized apatite, while in their inner parts Mn-oxide minerals and dufrénite occur in the form of needle-like radial aggregates (Selmeczi and Antal, 1974; Kubovics et al., 1989; Szabó and Vincze, 2013). Selmeczi and Antal (1974) reported microcrystalline quartz and albite formed syngenetically with apatite, with small rounded calcite inclusions occurring in the quartz grains.

The geochemical composition of the phosphorite is variable, depending on the apatite-Mn-oxide rich bands. U content of the apatite-rich phosphorite is between 300 and 700 ppm, furthermore it has a significant Be and REE content (200–500 ppm; Kubovics et al, 1989; Szabó and Vincze, 2013; Zajzon et al., 2014). In the phosphorite and attending massive Mn-oxide ores some chalcophile elements (Ag, Cd, Cu, Mo, Pb, Sb, Tl) also show small enrichment, while As and Zn can reach 1000 ppm (Kubovics et al., 1989; Polgári et al., 2000; Zajzon et al., 2014). Other elements, like Co, Li, V and W also show some enrichment compared to the host rock. Samples with higher concentration of Mn-oxide have higher content of the above mentioned elements and are enriched significantly also in Ba, Sr. Unique U-Be-HREE minerals occur only in traces, most of the U-Be-HREE is built into the structure of fluorapatite in inhomogeneous dispersion. Mn-oxide have often higher Be-content and also show enrichment in Li, while fluorophlogophite has the highest Li-content (Zajzon et al., 2014). Mn-oxide minerals probably incorporate the As, Ag, Cd, Co, Cu, Mo, Pb, Sb, Tl, V, W and Zn to their crystal structure because unique mineral phases from them are not yet identified (Polgári et al., 2000; Zajzon et al., 2014).

3. Samples and methods

3.1. Samples

Besides recently collected samples we used some samples collected earlier from the only known surface occurrence, excavation No. 40 (Fig. 1). A total of ten samples were investigated. Eight samples represent the different parts of the phosphorite and one sample (the ninth) comes from the host rock collected just above the excavation. During the sampling we found a dark, strongly folded 30 cm wide band containing small, maximum 15 cm wide, discus-like massive phosphorite lenses in an earthy, Mn-rich clay-bearing matrix. Each lens has a different structure, and the only common feature occurs at their edges as strongly brecciated parts, which contain fragments of a siliceous rock in 1–20 mm size. The small clasts of this siliceous rock occur also in the earthy mass, so we investigated one sample (tenth) from it as well. Representative samples are shown in Fig. 3. The description of samples and the investigations used are summarized in Table 1. Representative thin sections and characteristic banded-folded micro-texture of profiles are shown in Fig. 4.

3.2. Methods

Petrographic structural-textural studies were made on ten thin sections, in transmitted light (NIKON SMZ800 microscope and NIKON ECLIPSE 600 rock microscope, Institute for Geological and

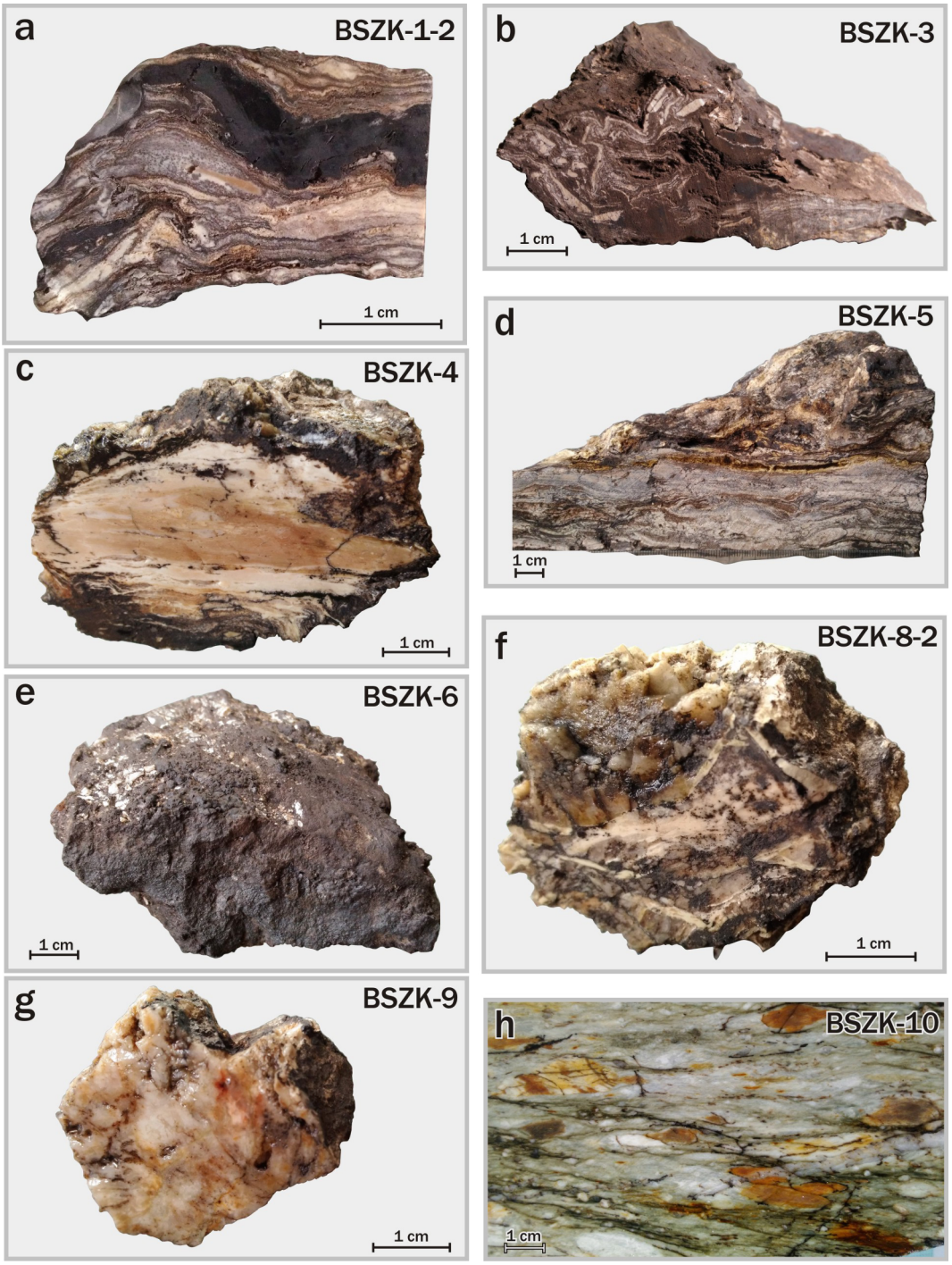

Fig. 3. Representative samples, massive part of a phosphorite layer. The ingredients are very fine-grained, only light and dark bands are observable.

Geochemical, Research Centre for Astronomy and Earth Sciences – IGGR RCAES – Budapest, Hungary). 600 photos and 3 panorama photo series of representative sections were taken.

Cathodoluminescence (CL) petrography was carried out on a thin section (Bszk-1–2) using a Reliotron cold cathode cathodoluminescence apparatus mounted on a BX-43 Olympus polarization microscope (Szeged University, Dept. of Mineralogy, Geochemistry and Petrology). Accelerating voltage was 7–7.7 keV during the analysis. Cathodoluminescence spectra were recorded using an Ocean Optics USB2000 + VIS-NIR spectrometer. Spectrometer specifications are 350–1000 nm wavelength range and 1.5 nm (FWHM) optical resolution.

Bulk mineralogical compositions of the samples (XRD) were analyzed by a Rigaku Miniflex-600 X-ray diffractometer with CuKα radiation equipped with a graphite monochromator at 40 kV and 15 mA. 'Random powder' samples were scanned with a step size of 0.05° 2 theta and counting time of 1 s per step over a measuring range of 2 to 70° 2 theta (IGGR RCAES, Budapest, Hungary). Mineral composition was determined on randomly oriented powdered samples by semi-quantitative phase analysis using a modified method of Bárdossy et al., (1980) and previously defined intensity factors. Mineralogical analyses were performed on 11 bulk samples.

Table 1
Description of samples collected from Excavation No 40, sampling data and the used investigations.

Sample ID	Thin section ID	Sub sample for XRD	Description	Methods					
				OM	CL	SEM-EPMA-EDS	XRD	Raman	FTIR
Bszk-1	**Bszk-1-1**	a,b	microlaminated phosphorite with white and dark brown bands (separated to: 1a - dark brown bands, 1b- white bands)	x		x	x		
	Bszk-1-2		duplication of 1–1, other half of the cut surface	x	x	x		x	x
Bszk -2	**Bszk-2**		microlaminated phosphorite with a thick, white, massive, Mn-oxide spotted part	x		x	x		x
Bszk-3	**Bszk-3**		strongly folded, microlaminated phosphorite with dominantly brown bands	x			x		x
Bszk-4	**Bszk-4**		white, massive phosphorite with a brecciated, Mn-oxide richer edge containing fragments of a siliceous rock	x			x		x
Bszk-5	**Bszk-5**	a, b, c	microlaminated phosphorite with white, yellowish and dark brown bands (separated to: 5a - whole sample, 5b - yellowish bands, 5c - white bands)	x			x		x
Bszk-6			Mn-enriched dark gray lens, massive Mn-oxide ore with small phosphorite fragments				x		
Bszk-7			Mn-enriched dark gray lens, massive Mn-oxide ore				x		
Bszk-8	**Bszk-8-1**		white, thin massive phosphorite with a wide brecciated edge containing fragments of a siliceous rock	x			x		
	Bszk-8-2		white, thin massive phosphorite with a wide brecciated edge containing fragments of a siliceous rock	x					
	Bszk-8-3		white, thin massive phosphorite with a wide brecciated edge containing fragments of a siliceous rock	x					
Bszk-9	**Bszk-9**		massive or sometimes porous, partly coarse-grained gray siliceous rock with small sericite aggregates	x					
Bszk-10	**Bszk-10**		host rock pyroclastic material metamorphosed to light green sericite shale with porpyry quartz/alkaline feldspars and white/brown colored, elongated silicified lenses	x					

Abbrev.: OM: optical rock microscopy; CL: cathodoluminescence microscopy; SEM-EPMA-EDS: scanning electron microscopy; XRD: X-ray powder diffractometry; Raman: Raman spectroscopy; FTIR: infrared spectroscopy. Samples were collected at 9, March 2017.

Element composition and micro-textural features of 1 thin section (Bszk-1) were determined by SEM-EDS used to determine micro-textural features and mineral composition on samples by an AMRAY 1830 SEM equipped with an EDAX PV9800 EDS detector, at Eötvös University, Dept. Petrology and Geochemistry, Budapest. Conditions of analyses were the following: accelerating voltage 20 kV, beam current 1nA, electron beam diameter ~ 50 nm (focused beam), measurement time 100 s lifetime. Amelia AS5010-AB albite, MAD-10 orthoclase, Glen Innes, Australia, C. M. Taylor Company kaersutite, LP-6 biotite, C. M. Taylor Company diopside international standards were used.

Element composition and micro-textural features of 2 thin sections were determined at 1–2 μm spatial resolution on carbon-coated samples using a JEOL Superprobe 733 electron microprobe with an INCA Energy 200 Oxford Instrument Energy Dispersive Spectrometer, run at 20 keV acceleration voltage, 6nA beam current and count time of 60 s for the spot measurement and 5 min for line-scan analysis. Olivine, albite, plagioclase and wollastonite standards were used; we estimated that the detection limit for the main elements was below 0.5% based on earlier measurements with various samples (IGGR RCAES, Budapest, Hungary). A total of 80 spectra were acquired, and 66 backscattered electron images were made.

Fourier transform infrared spectrometer (FTIR) was used for *in situ* micro-mineralogy and organic material identification on five thin sections (145 spectra, IGGR RCAES, Budapest, Hungary), using a Bruker FTIR VERTEX 70 equipped with a Bruker HYPERION 2000 microscope with a 20x ATR objective and MCT-A detector. During attenuated total reflectance Fourier transform infrared spectroscopy (ATR) analysis, the samples were contacted with a Ge crystal (0.5 μm) tip with 1 N pressure. The measurement was conducted for 32 s in the 600–4000 cm^{-1} range with 4 cm^{-1} resolution. Opus 5.5 software was used to evaluate the data. The equipment cannot be used for Mn-oxide determination because those peaks fall in the < 600 cm^{-1} range. Contamination by epoxy glue, glass, wood stick, and dichloromethane was taken into consideration. The sample name was marked by graphite on the rim of the sample, in epoxy resin, which was eliminated from the interpretation.

High resolution *in situ* micro-Raman spectroscopy was used for micro-mineralogy and organic matter identification on a representative thin section (Szeged University, Hungary). The Bükkszentkereszt profile (Bszk-2) contains a total of 1800 Raman spectra, the spectra were measured at step-sizes of 10 μm. The profile is distributed over four sections, each section containing a length of 4.5 mm (450 spectra). The sections are as follows: section 1 (10–4,500 μm), section 2 (4,510–9,000 μm), section 3 (9,010–13,500 μm), section 4 (13,510–18,000 μm). A Thermo Scientific DXR Raman Microscope was used, with a 532 nm (green) diode pumped solid-state (DPSS) Nd-YAG laser using 1.5 mW laser power and 50x objective lens in confocal mode (confocal aperture 25 μm slit). Acquisition time was 1 min and spectral resolution was ~ 2 cm^{-1} at each measurement; the distance between each point was 10 μm and the measurement time was 10 min. A composite image of thin sections of Raman microscopy measurements and series of Raman spectra acquired along the vertical sections are indicated on thin section photo in results section (arrow points to measurement direction). Diagrams were organized on peak height versus analytical spot number of each of the phases along the Raman scanned section. Intensities were normalized to the highest peak for each spectrum. The following Raman bands were used for normalization: quartz: ~463 cm^{-1}; goethite: ≃390 cm^{-1}; hollandite: ≃580 cm^{-1}; groutite/manganite: ≃554 cm^{-1}; cryptomelane: ≃184 cm^{-1}; carbonaceous matter: ~1605 cm^{-1}. Identification of minerals was made with the RRUFF Database (Database of Raman – spectroscopy, X-ray diffraction, and chemistry of minerals: http://rruff.info/). Contamination by epoxy glue was taken into consideration. The sample name was marked by graphite on the rim of the sample, in epoxy resin, and this was also eliminated from the interpretation.

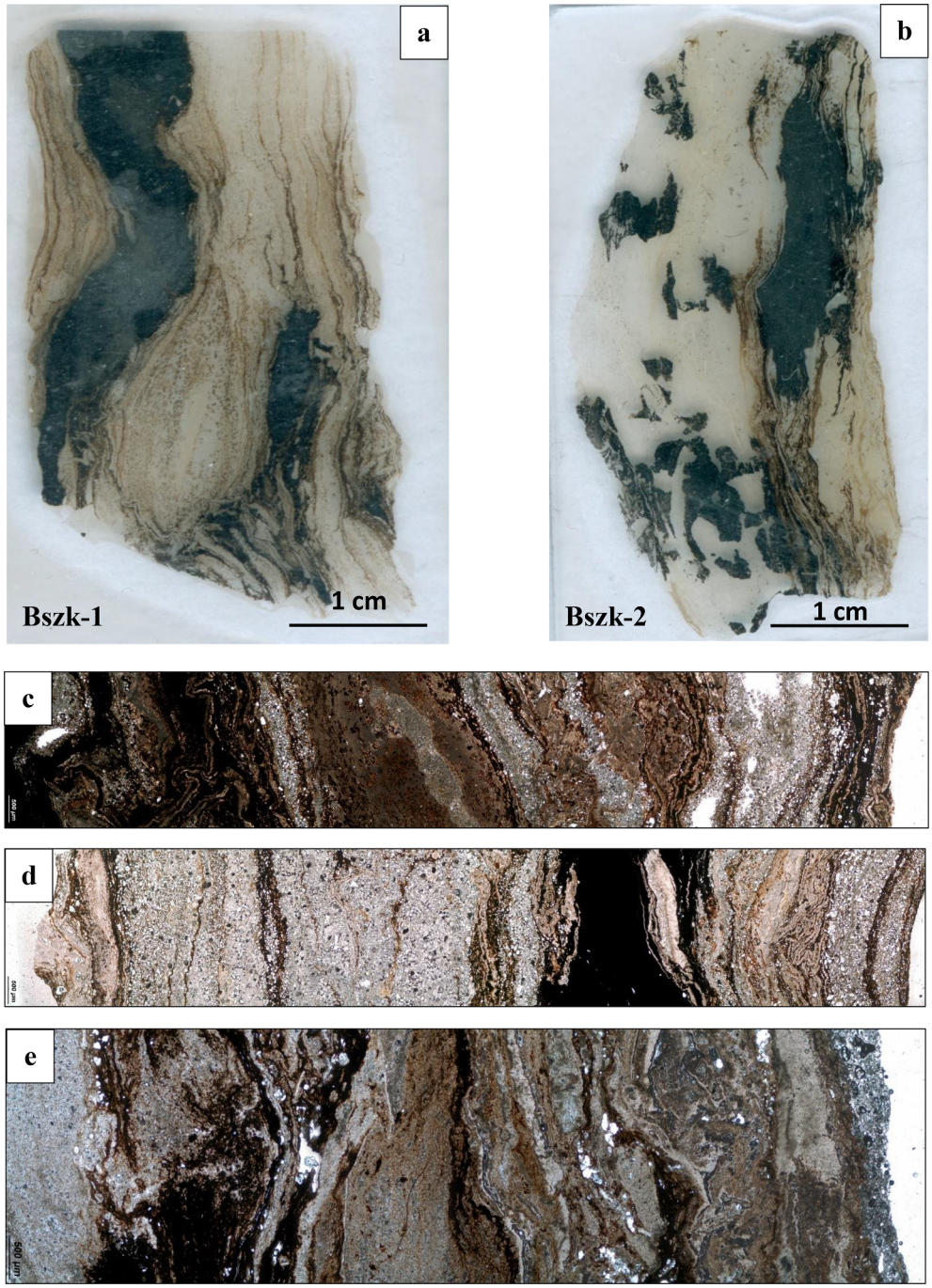

Fig. 4. Representative thin sections (a-b), and characteristic banded-folded micro-texture of profiles (c) Bszk-1, (d) Bszk-1-2 and (e) Bszk-2 (petrographic microscope, transmitted light).

4. Results

4.1. Rock microscopy, CL and SEM-EDS

4.1.1. Rock microscopy

The thin sections represent variable micro-textural features and mineralogy (Figs. 5–8). A macroscopic description is shown in Table 1.

4.1.1.1. Host rock. The sample Bszk-10 shows a strong shear deformation structure, the matrix is fine grained quartz and mica (sericite) in the form of thin bands. The 1–3 mm sized quartz and feldspar porphyroclasts are often broken, strongly sheared, the quartz grains often show undulatory extinction or dynamic recrystallization and form sigma clasts. The presence of sub-grains is also a common phenomenon, while the feldspar grains show breaking structure only. The elongated lenses, 2–5 cm in size, are made up also from quartz and mica, but have a different micro-texture than the matrix (Fig. 5ab): they mostly represent altered pumices (Fig. 5ab) and sometimes coarse-grained quartz-feldspar bearing lithic clasts (Fig. 5c). A few zircon crystals and limonite pseudomorphs after pyrite also occur.

4.1.1.2. Siliceous rock. The sample Bszk-9 is built of crypto- and microcrystalline quartz with laminar mica (sericite) aggregates, the coarse-grained parts are aggregates of spheric structures of approximately 10–50 μm (Fig. 5d, 8e-f); from their positive sign of elongation behaviour they are quartzine, not chalcedony. The rock

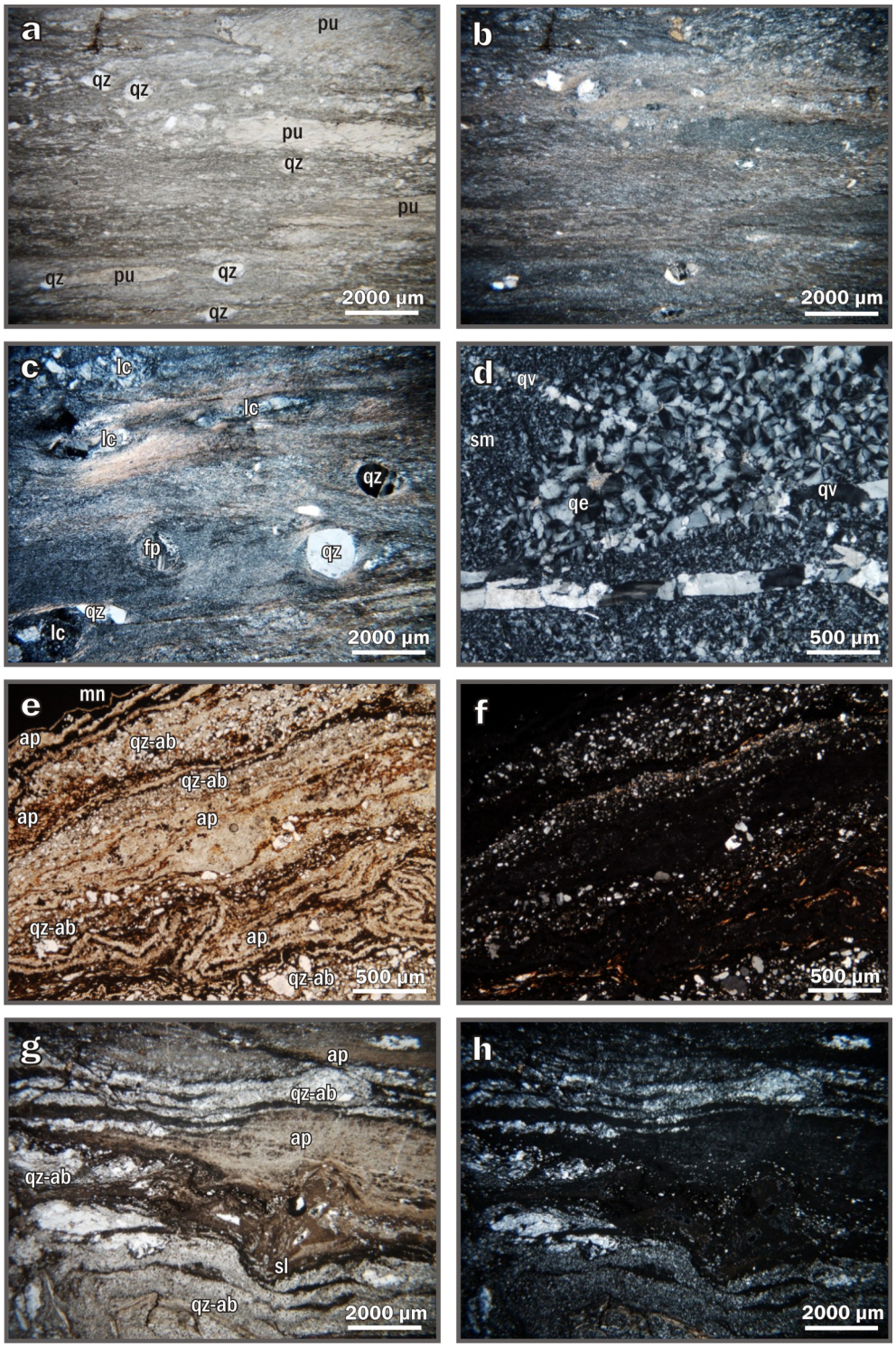

Fig. 5. (a-c) Remnants of pyroclastic texture elements in host rock: porphyric quartz (qz) and feldspar (fp) crystals, altered pumices (pu) in form of lighter lenses, which have different material and texture than the matrix, altered lithic clasts (lc). Typical metamorphic features are the foliation of the matrix and the undulatory extinction and dynamic recrystallization of quartz grains. (d) Typical texture of the siliceous rock, coarse-grained part in fine-grained siliceous matrix (sm) with coarse-grained quartz fissure fillings. The spherical quartzine material (qe) of the coarse-grained part seems to resorb the earlier quartz veins (qv). (e-f) Microlaminal ribbon-like parallel folded and broken texture; laminae that are apatite-rich (ap) are fine-grained, cream-coloured and remain black by cross-polarization, the other laminae are rich in coarser diagenetic quartz-albite grains (qz-ab) along woven structure and a Mn-oxide rich band (mn). (g-h) Synsediment sliding of an apatite-rich band with chaotic inner structure through a diagenetic quartz-rich band. Homogenous apatite (ap) filled this sliding structure (sl) from the right edge, the neighbouring coarser quartz-rich band (qz-ab) is not folded. Samples: Bszk-10: a-c, Bszk-9: d, Bszk-1: e-f, Bszk-5: g-h (photos made by optical rock microscope, transmitted light, a, e, g – 1 Nicol, b-d, f, h – crossed Nicol).

contains several generations of quartz: porphyric crystals and quartzine, quartz veins and coarse-grained quartz clasts partly altered to quartzine, and fresh coarse-grained veins which crosscut the quartzine (Fig. 5d). The quartz and the quartzine show similar deformation features as the Bszk-10 sample described above, forming sub-grains is the most typical feature. Small amounts of zircon crystals and goethite pseudomorph after pyrite also occur.

4.1.1.3. Phosphorite. The phosphorite samples show a complex forming history with features of many deformation phases. We classified the observed and definable textural features into four stages: a synsediment phase, an early diagenetic, and two deformation phases, one close in time to the synsediment processes and one far later in geological time, mostly in connection with metamorphism.

Synsedimentary and early diagenetic features

Light cream coloured, beige ribbon-like parallel, sometimes folded and/or broken laminae of especially fine-grained apatite are characteristic. The laminae are built up from radial needle-like fibrous apatite crystals (Figs. 4, 5e-h, 7a, 9).

Along the woven structures and also ribbon-like laminae coarser grains (10–100 µm) of quartz and albite occur, with small laminae of

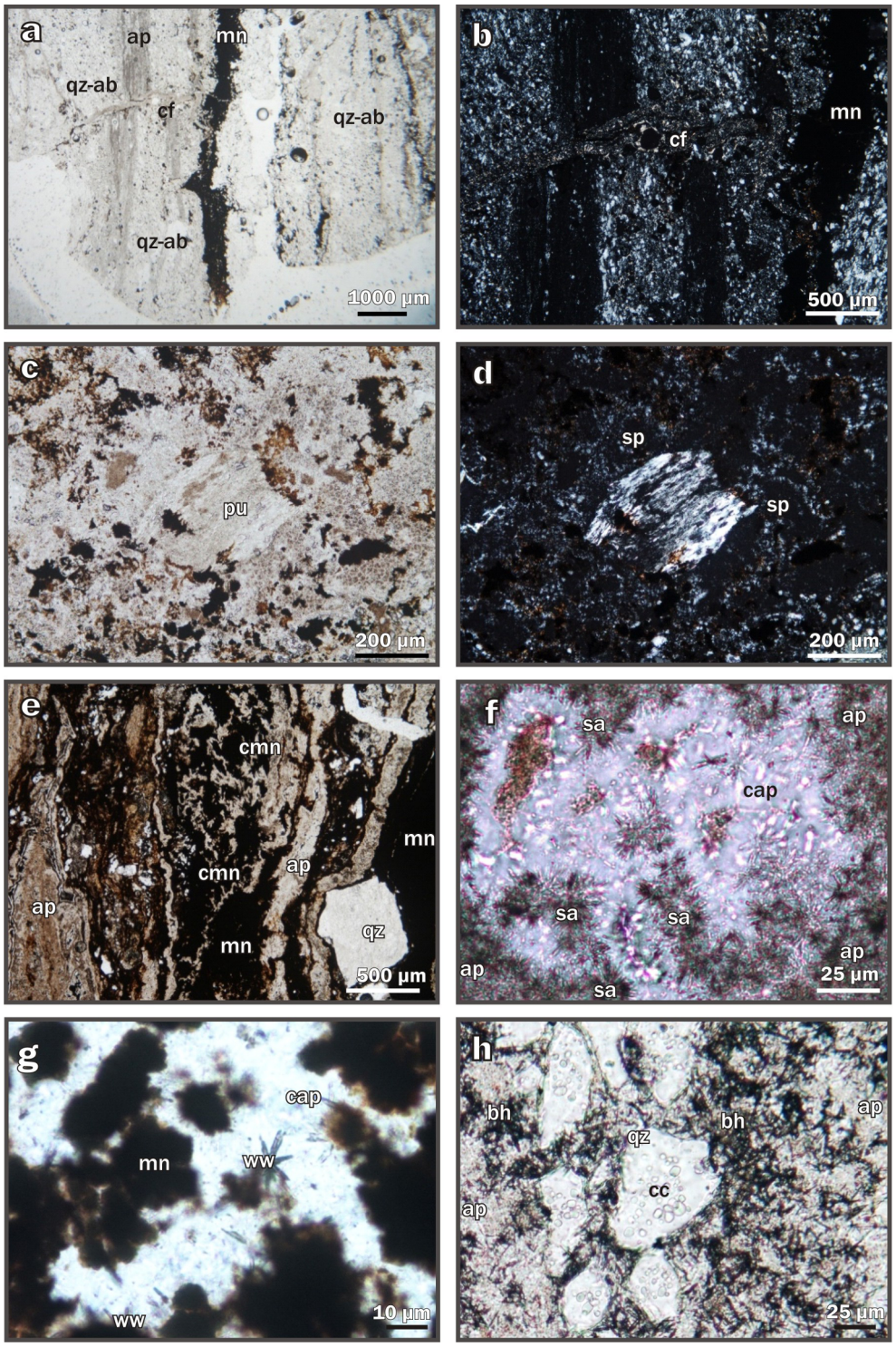

Fig. 6. (a-b) Small synsediment fault, active before the forming of the Mn-oxide rich layer (mn), the crack is filled with mica and apatite rich fine-grained material (cf). (c-d) Mica-filled altered pumice (pu) retaining the filamentous structure. The phosphorite matrix shows micro-spherolitic structure (ms) under crossed polarisers. Rims of the spherolites (sp) consist of secondary crystalline apatite, visible under crossed polarisers. (e) Pressed phosphorite bands around huge quartz porphyroclast (qz). Different occurrence of Mn-oxides (mn), massive bands (mn), and irregular aggregates of needle-like crystals (cmn), and biomat structure of apatite rich laminae (ap). (f) Vermiform, filamentous structures form spherical aggregates (sa) in fine-grained apatite (ap) as observed at high magnification. The white mass is secondary crystalline apatite (cap). (g) Whewellite star (ww) in crystalline apatite (cap) and spherical opaque aggregates, mostly made up of Mn-oxides (mn). (h) Irregular aggregates of needle-like opaque berthierite (bh) in the fine-grained apatite (ap) matrix and resorbed diagenetic quartz (qz) crystals with calcite inclusions (ca). Samples: Bszk-8-3: a-b, h, Bszk-4: c-d, Bszk-5: e, Bszk-3: f, g (photos made by optical rock microscope, transmitted light, a, c, e-h – 1 Nicol, b, d – crossed Nicol).

a mica mineral in their matrix representing debris-like micro-laminae (Fig. 5e-h, 6a-b, e, 8a-d), and causing the laminated microtexture. These grains and the mica laminae can also grow sparsely in apatite-rich bands.

Occasionally coarser, 100–500 µm large porphyric crystals (quartz and K-feldspar) and volcanic rock fragments can be seen (lithic clasts, totally altered pumices and bone-like shaped glass shards; Fig. 6c-e). In a few instances, it seems that the large grains exert pressure against the neighbouring bands (Fig. 6e). Small zircon crystals also occur sparsely.

Intense phosphatisation of tuff remnants, pumice, volcanic glass, and other breccia particles is common.

Fluffy, spheroidal clusters (biosignatures) of fine-grained apatite are shown in Fig. 6d and f. Sometimes within this kind of apatite, almost opaque stars built up from needles of whewellite occur (Fig. 6g-h). Brown woven, limonite-rich structures forming series of biomat-like and stromatolitic structures are common (mineralized biosignatures of putative Fe-oxidizing bacteria (FeOB; Fig. 7a, 8a).

At very high resolution (100–1000x), the whole sample shows a densely woven fabric with filamentous, inner necklace-like microstructures or coccoid forms, aggregates and vermiform brain-like micro-textures (mineralized biosignatures). These filaments contain

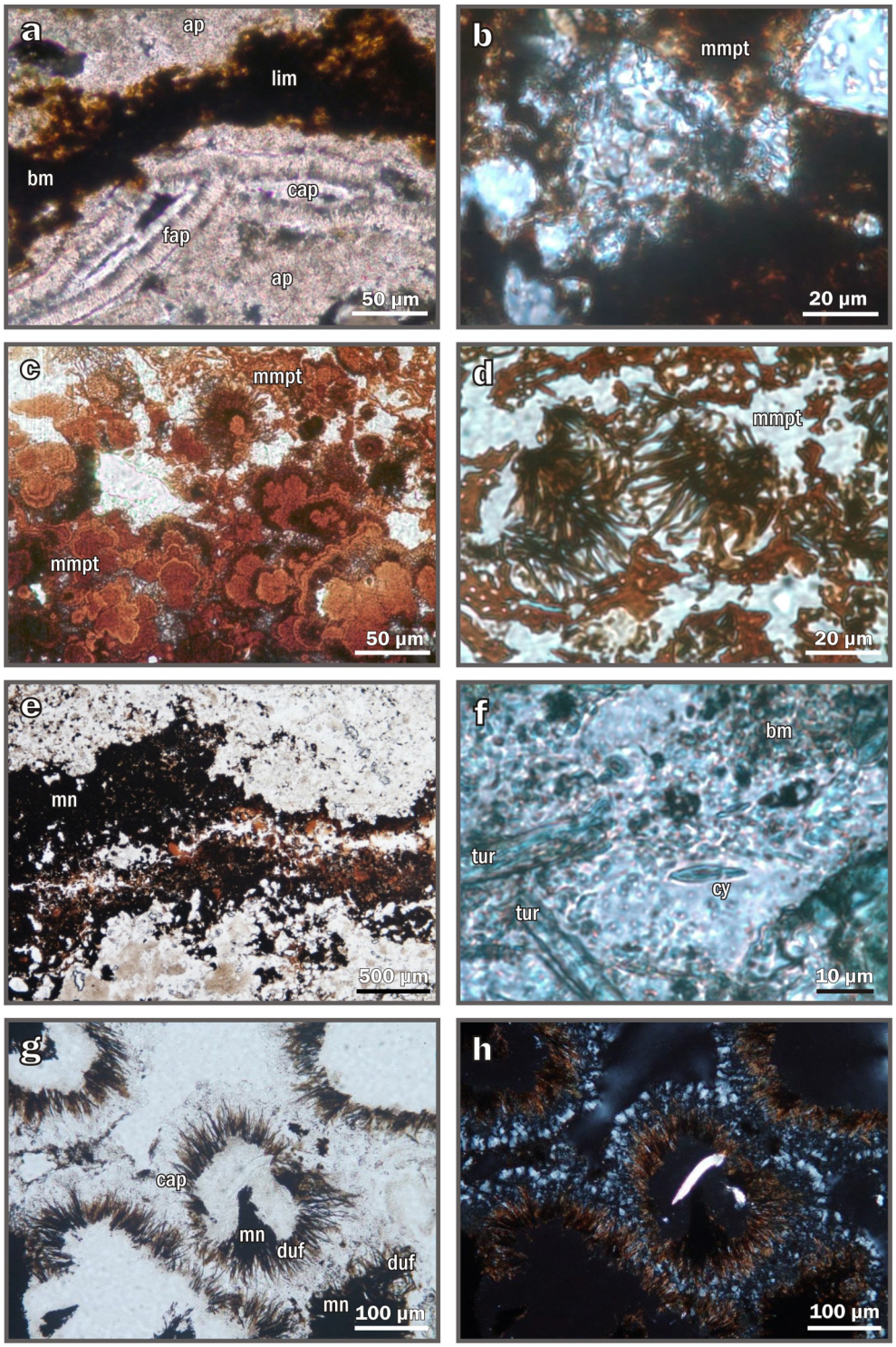

Fig. 7. (a) Brown woven limonite-rich biomat-like stuctures (lim, bm) in a fine-grained apatite rich band (ap). All parts show densely woven filamentous and vermiform micro-textures. The apatite laminae are built up from axial needle-like fibrous apatite crystals (fap), with secondary apatite crystals (cap) in their fissures. (b) Mineralized microbially produced textures such as filamentous, pearl-necklace-like, vermiform forms, sometimes coccoid-like aggregates (mmpt). (c-e) Reddish-brown concentric and stromatolitic biosignatures made up of ferrihydrite (mmpt) occur in some Mn-oxide rich bands (mn) and are visible only in thinner parts of the thin section, with the concentric forms being individual iron-oxidizing bacteria in the form of vermiform filaments (arrow). (f) Cyanobacteria-like form (cy) with needles of diagenetic tourmaline (tur) and biomat (bm) in a fine-grained silica matrix (putative cyanobacteria are shown based on similarity published by Gyollai et al., (2015) on Namibian Neoproterozoic sample). (g-h) Translucent to opaque dufrénite (duf) needles form radial texture around pores, partly filled with Mn-oxide (mn) (black). Prismatic apatite crystals (cap) cover the dufrénite. Samples: Bszk-2: a, Bszk-1: b, Bszk-3: c-d, Bszk-8–2: e, Bszk-4: f, Bszk-5: g-h (photos made by optical rock microscope, transmitted light, a-g – 1 Nicol, h – crossed Nicol).

0.5–1 µm large orange balls. They belong to the very fine-grained apatite and limonite phase as well (in the apatite they are more easily visible; Fig. 6g, 7a-b).

Reddish-brown concentric forms connected to Mn-oxide bands in some thin sections are also very common. They are only visible in the thinnest parts, like the edge of the thin sections. Among them, also reddish-brown filamentous colonies occur with a complex pearl-necklace-like inner texture, and also coccoid-like aggregates, which are much bigger than in the similar forms in the apatite-limonite rich bands (Fig. 6a, 7c-e). The thin vermiform filaments contain orange coloured balls below the size of 1 µm. The filamentous, fibrous phases form axial or randomly oriented woven, vermiform micro-textures. The concentric micro-texture often has a stromatolitic character.

Rarely mineralized cyanobacteria-like biosignatures occur (Fig. 7f). The length of the biosignatures is around 20 µm, the width is 5 µm. Needle-like radial or randomly oriented opaque minerals (Mn-oxide), as well as translucent needle-like minerals (duphrènite) occur, commonly in connection with spheric structures (Fig. 7g-h). In quartz grains (20–100 µm) of debris-like bands, numerous small calcite inclusions of µm size often occur. However, we found that rarely albite can also contain them and quartz and albite further

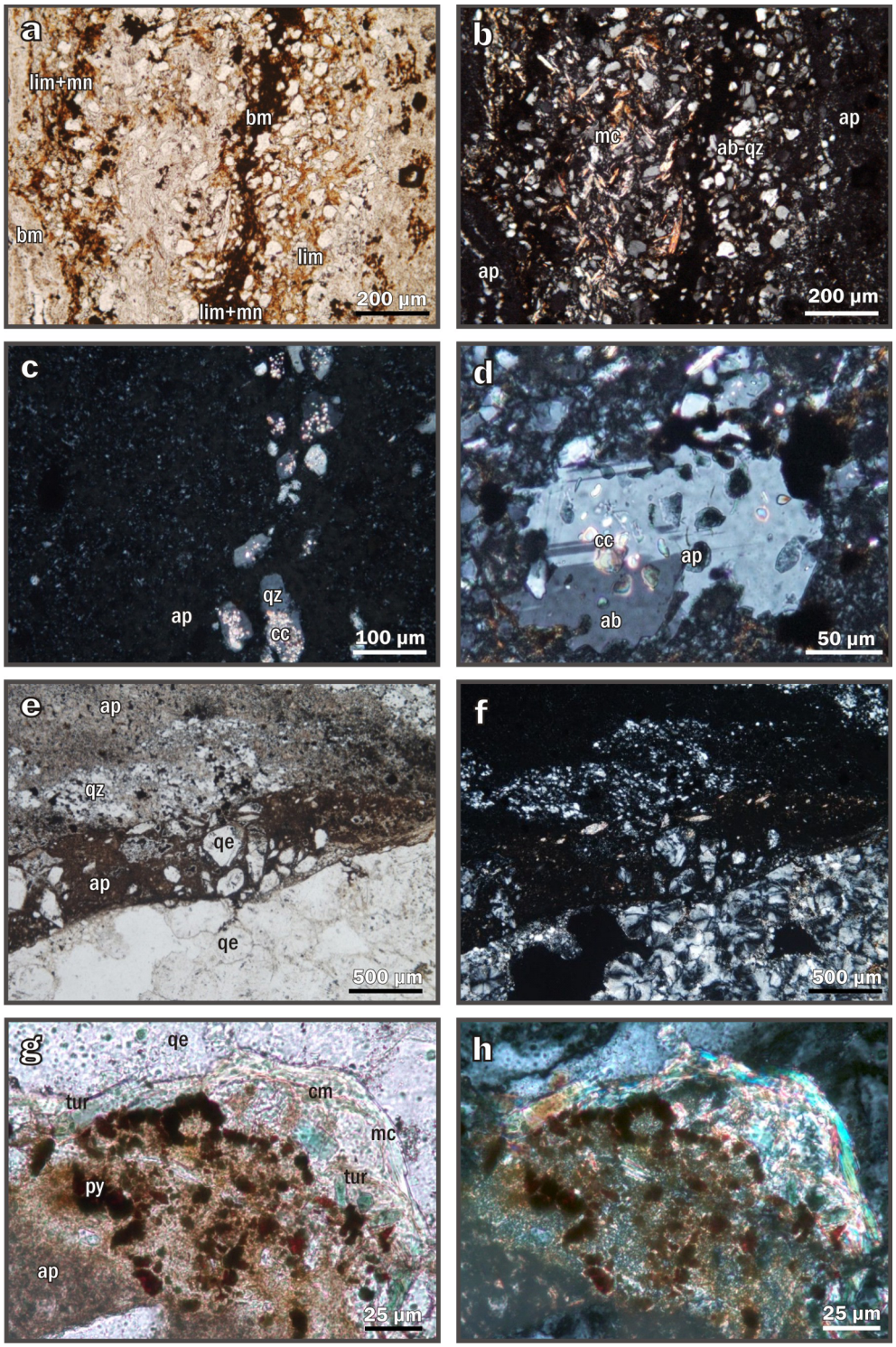

Fig. 8. (a-b) Coarse-grained, diagenetic albite-quartz bearing band (ab-qz) with mica (mc) matrix, also containing Mn-oxide cementation and limonite-rich biomat-like structures (lim + mn, bm). (c) Resorbed diagenetic quartz crystals (qz) with small calcite (cc) inclusions in a fine-grained microspherolitic apatite (ap) matrix. (d) Resorbed albite crystal (ab) with calcite (cc) and phosphorite inclusions (ap) (blurred green inclusions at cross polarization). (e-f) Brecciated edge of the phosphorite, clasts of the spherical quartzine-bearing siliceous rock (qe) cemented by cream-like fine-grained apatite (ap). (g-h) Border zone of an apatite-rich band (ap) and a siliceous clast (qe); mica (mc) and limonite pseudomorphs after pyrite (py) occur with greenish prismatic tourmaline (tur) crystals and greenish clay mineral (cm) aggregates. Samples: Bszk-1: a-b, Bszk-8–3: c-d, Bszk-8–1: e-f, Bszk-4: g-h (photos made by optical rock microscope, transmitted light, a, e, g – 1 Nicol, b-d, f, h – crossed Nicol).

contain similar sized phosphorite inclusions, too (fragments of cryptocrystalline apatite). The including diagenetic quartz and albite form xenomorphic-hypidiomorphic grains. Quartz typically contains inclusions in an apatite-rich environment. In a quartz-albite-mica-rich environment, quartz grains rarely contain these inclusions. Often these grains are strongly resorbed during diagenesis (Fig. 6h, 8c-d).

Early deformation features (synsediment or a little bit later)

Randomly spilled out bands (Fig. 4.), breaks, brecciation, and folds affect only some bands. Micro-faults are filled up with mica-rich material (Fig. 5g-h, 6a-b).

Apatite-rich bands contain thin veins with crystalline apatite fissure fillings, in the form of prismatic crystals. These veins irregularly net the apatite-rich bands, and typically they do not enter the quartz-albite-mica-rich bands.

Brecciation is a common feature at the edges of the phosphorite layers: the edges contain a lot of irregularly shaped clasts in the size of some centimeters, the clasts are from the different bands of the phosphorite and from the siliceous rock (Fig. 8e-f). Between the brecciated clasts, fine-grained apatite and Mn-oxide cementation

occurs. The apatite cementation has the same textural features as the cryptocrystalline, “micro-spherulitic” apatite bands.
Greenish-blue translucent columnar minerals (length is variable but up to 100 μm, the cross section is around 20 μm), most probably tourmaline, are also characteristic of the brecciated zone, in mica enriched zones of the siliceous rock (vein fillings and edge of clasts towards apatite-rich zones). Around and inside the tourmaline, mineralized microbial biosignatures occur (Fig. 7f). Tourmaline-mica-rich parts are sometimes associated with limonite pseudomorphs after pyrite in 10 μm size (Fig. 8g-h).

Metamorphic and other deformation features in geological time

Folding affecting all of the bands is often observable, which is associated with shear features. Brecciation affects the inner bands of the phosphorite. Lenses of varying thickness occur anywhere between the phosphorite bands, which are filled by clasts from the phosphorite and well-foliated pieces from the metamorphosed rhyolitic host rock, also as a result of shear deformation (Fig. 4).
The same deformation features are observable in the different quartz appearances of the phosphorite (coarse-grained parts of siliceous clasts, bigger-smaller, inclusion-bearing grains in phosphorite bands, porphyric volcanoclasts). Undulatory extinction or dynamic recrystallization of larger quartz grains and their disintegration into sub-grains along a loba-like suture are also common features.
Presence of oriented micas.
Secondary Mn-oxide occurs as bands with irregular borders, crack fillings, dendritic structures or opaque, solid lense-like over-writings (Fig. 4, 6e, 7e).

Undefinable, general secondary (later) features

Second generation apatite forming prismatic crystals occur in fissure fillings of apatite laminae and the micro-spherulitic structures often have a well-crystallised apatite rim (Fig. 7a, h).
Sericitization of K-feldspar porphyroclasts and albitization on their edges occur – Na incorporation (substitution), metasomatism-like effects.

4.1.2. Cathodoluminescence (CL)

Apatite-bearing woven structures and thinner and thicker biomats, as well as very fine grained phases (as well as stromatolite-like structures; Fig. 9a-d), show bright yellow luminescence (Fig. 9e-f). The spectra are taken from the apatite, support REE (Dy^{3+}, Sm^{3+}, Eu^{3+}, Pr^{3+}, Mn^{2+}, and UO_2) as activator elements (Fig. 9g, h).

The debris-like quartz grains show only a weak brownish luminescence and the albite grains do not show luminescence in spite of their quartz and feldspar mineralogy (Fig. 9e). The fine grained carbonate inclusions in quartz crystals show bright orange luminescence (Fig. 9e-f). Some kinds of apatite (secondary, well crystalline) can show blue luminescence (Fig. 9e).

4.1.3. SEM-EDS

The micro-lamination and the woven, biofilm-/biomat-like textures are clearly visible in Fig. 10a, b, Fig. 11d, e. The minerals are very fine grained and mixed, Fe-bearing clay along biomats (Fig. 12e, f), apatite (Fig. 10f, 11a, b, d, e, and f, 12e, f) and Mn oxides occur (K-bearing, sometimes K- and Ca-bearing; Fig. 11a, b, c, 12c, d). Apatite and Mn oxide form a fine-grained mixture. Mn oxide also occurs as a fine, needle-like mineral (Fig. 10b, e, f, and 12b, c). Poorly crystallized parts contain traces of Mn, K, Ca, and P, while and in their vicinity a Mn-, K-, Ca-bearing phase occurs without P, fine needle-like apatite is common (Fig. 12d). Fine-grained apatite also mixes with Fe-bearing clay, and also forms more compact ribbon-like phases (Fig. 12e). Coarser apatite (Fig. 10e, 11c) and phyllosilicate grains also occur. This phyllosilicate-rich zone (detrital-like quartz-feldspar-mica) appears between a fine-grained apatite-rich band (gray) and a Mn oxide-rich (light) band. The Mn oxide-rich layer seems to be homogenous by optical microscopy, but closer examination shows that it consists of a mixture of fine-grained Mn oxide, apatite, and other components (Fig. 11a, b). Debris-like clasts are characteristic with quartz being the main type (Fig. 10c, f, 12e), Fe-rich grains are sub-ordinate (Fig. 10d, 11f). Quartz often includes smaller calcite grains (a few μm in length; Fig. 11f).

4.2. Bulk mineralogy (XRD)

Three groups were distinguished based on the mineral assemblages (Table 2). Bszk-4, Bszk-5a, Bszk-5c, and Bszk-8-1 belong to the first group. These samples contain only quartz and apatite.

Bszk-6 and Bszk-7 belong to the second group. This group contains various manganese oxide minerals. The main mineral phases are ramsdellite and pyrolusite, but this group contains todorokite and hollandite/birnessite in smaller amounts.

The third group, including Bszk-1a, Bszk-1b, Bszk-2, Bszk-3 and Bszk-5b, is composite, its main mineral phases are apatite, quartz, and feldspar. However, every sample contains small amounts of manganese oxide (todorokite, hollandite/birnessite). Bszk-1a and Bszk-1b contain 10 Å phyllosilicate, while Bszk-5b contains smectite.

4.3. FTIR in situ measurements

The mineral and variable organic matter content, distribution and frequency based on FTIR are summarized in Table 3. Besides random measuring points, measuring areas were chosen based on optical rock microscopy to identify mineral phases. Apatite, feldspar, quartz as main constituents, ferrihydrite, hematite, goethite, montmorillonite, tourmaline, whewellite, duphrénite as moderate components and beryllonite, and berthierite as trace accessories were detected.

Bszk-2 contains whewellite together with beryllonite and organic matter. Yellowish parts consist of Fe oxide and quartz, and the fine grained apatite is rich in duphrènite, and also coarser grained granular feldspar and quartz.

The biofilm-biomat-like structures have a mixed composition containing Fe oxides/hydroxides (ferrihydrite, hematite), and montmorillonite. Brownish-red stromatolitic parts contain ferrihydrite, quartz and organic matter (Bszk-3). Berthierite occurs as a black (opaque) needle-like mineral, while the translucent fibrous material is duphrènite, which also occurs in the vicinity of coarser grained apatite, albite, and a high amount of organic matter in Bszk-3. Whewellite also occurred in this sample in the form of star-like fibrous and needle-like aggregates (Fig. 6f-h).

Bszk-4 contains columnar tourmaline in the vicinity of fine grained ferrihydrite, in the coarser parts feldspar and duphrènite were detected; beryllonite rarely appears. Bszk-5 contains whewellite together with duphrènite, ferrihydrite, and hematite (yellowish parts). Various hydrocarbons were also detected as main components (aromatic hydrocarbon, carboxyl groups, and C–H stretching of aliphatic hydrocarbons) as well as OH, referring to water content.

4.4. Raman spectroscopy in situ measurements

Table 4 summarizes the frequency of mineral and also organic material phases, while Fig. 13 shows the distribution of the main mineral phases according to the profile (sample Bszk-1). Besides the sections, random point analyses were also made, which detected hematite, apatite, Mn oxide(s), and plagioclase.

Most of the mineral reference data (e.g., manjiroite, braunite, rhodochrosite, apatite, albite, quartz) were obtained from the RRUFF database (Lafuente et al., 2015; Table 4). The *manganese oxides* were identified in detail after Sepulveda et al., (2015) and Julien et al., (2004), whereas *iron minerals* were identified after Das and Hendry (2014). The vibration bands of *organic material* were identified after

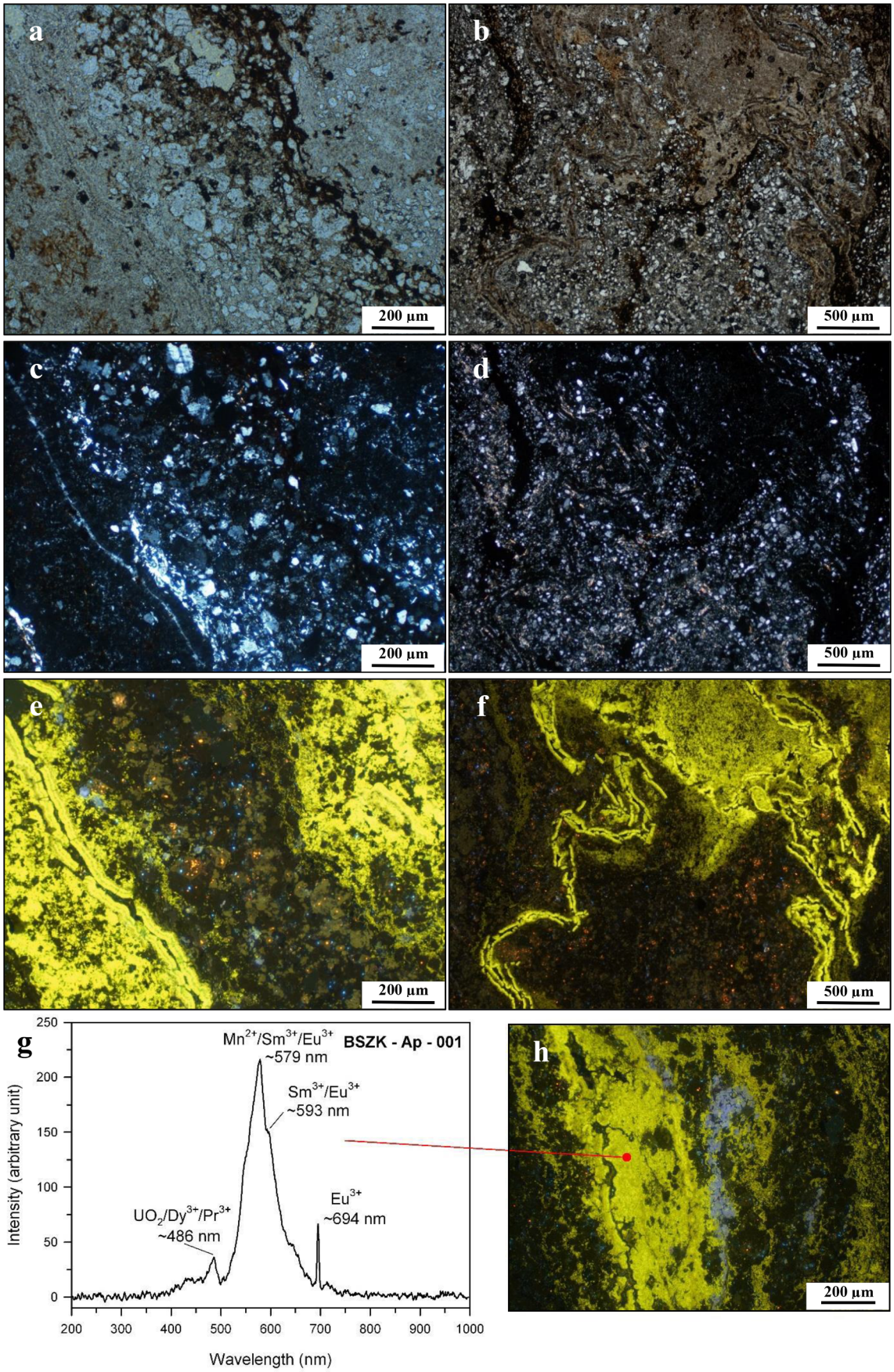

(caption on next page)

Fig. 9. Cathodoluminescence (CL) photos of sample Bszk-1. (a) Series of biofilms with debris-like micro-laminae, optical microscopy, 1 Nicol; (c) crossed Nicol, (e) CL photo. Apatite-bearing laminated structures as well as very fine-grained phases, broken biomats (as well as stromatolite-like structures) show bright yellow luminescence, while the coarse-grained, debris-like band of diagenetic quartz crystals display a brown luminescence. The bright orange spots are calcite inclusions. The diagenetic mineral-rich bands are almost apatite-free. (b) Light cream coloured, beige ribbon-like parallel, folded and broken laminae in coarse-grained quartz matrix, as signs of snysediment movements within bands, optical microscopy, 1 Nicol (d) crossed Nicol, (f) CL photo. Brown luminescence of quartz and bright orange calcite inclusion are also visible. (g) Spectrum acquired from apatite on (h), with activator elements; (h) CL photo, apatite shows bright yellow luminescence, the bluish colour probably indicates secondary apatite.

Okolo et al., (2015; aromatic ring 800–225 cm^{-1}), Jehlička et al., (2009; CH2-CH3 bands aliphatic hydrocarbon 1000–1487 cm^{-1}), Chen et al., (2007, 1600 cm^{-1} graphite), and Orange et al., (1996; PAHs – 1610–1680 cm^{-1} and long-chain hydrocarbons – 1700–2000 cm^{-1}). In total, 14 types of organic material were identified in the Bükkszentkereszt profile (Table 4).

The apatite, feldspar, and manganese oxides (cryptomelane, romanèchite/psilomelane, pyrolusite) are in most cases well crystallized, every vibration type was detected, whereas the other minerals showed only the main vibration types (marked “s” in the table). Detailed elaboration of the spectra yielded the following mineral and organic matter compositions in the sections, as specified in Fig. 14.

Section 1:

The first mm consists of apatite albite lamination, where the cycles vary between 10 and 50 μm. Several laminae in first 100 μm contain braunite. Nontronite (860 μm) and montmorillonite (830, 960 μm) also occur. The second mm contains the coexistence of Mn-oxides: manganite and cryptomelane, whereas manjiroite tends to occur in the first mm of the layers. Iron oxides were detected between 750 and 820 μm. 10 types of organic materials were detected between 0 and 1100 μm with 10–30 μm thick cycles. Between 2200 and 4400 μm the section consists of cryptomelane and manganite, and in last 100 μm pyrolusite, birnessite was detected. The section contains several cycles of organic material (most common types: org 8, org 10) and between 3,370–4,410 μm the organic fraction is graphite with manganese oxide. Quartz occurs at 40 and at 4,420 μm.

Section 2

Between 4510 and 4630 μm the section contains manjiroite, cryptomelane, birnessite with 20 μm thick intersections of cryptomelane and psilomelane, with 20–50 μm thick cycles of organic material (graphite, type org 10). Between 4,640–4,690 μm manganese ore was not detected. Between 4,720–5,210 μm the manganese indication consists of manganite and cryptomelane, and variable intersections with apatite. Between 5,220–5,320 μm cryptomelane occurs. The section between 5,350–5,430 μm contains iron oxide layers of ferrihydrite, goethite and lepidocrocite with organic material, while the 5,330–5,790 μm section consists of manjiroite, cryptomelane, romanéchite (psilomelane), and pyrolusite with cycles of 10–150 μm. The organic material occurs only with manganese oxide. Above 6,000 μm, apatite layers (occasionally with albite) occur (30–500 μm cycles).The lamination of organic material varies between 10 and 70 μm). Quartz occurs at 7,280 and 7,290 μm (frequent), and at 7,310 and 7,450 μm. Rhodochrosite occurs at 7,540–7,570 μm and at 7,630–7,640 μm.

Section 3

This section consists of apatite with a 20–80 μm intersection of manganese oxides (cryptomelane, romanéchite (psilomelane) and 10 μm manjiroite. Together with cryptomelane, occasionally 20–40 μm thick iron oxide layers were detected (lepidocrocite, hematite, goethite). Montmorillonite occurs at 12,000 μm, quartz at 11,750 μm.

Section 4

Between 13,510 and 13,690 μm, the apatite layers are intercalated with 20–50 μm thick layers of manganese oxides (romanéchite (psilomelane), cryptomelane, and manjiroite), with traces of quartz, uranyl-sulfate (johannite) and iron oxide (ferrihydrite, hematite), and 10–30 μm thick laminae of organic material (types: graphite, org 1, org 2). From 13,690 μm to 13,750 μm, manganese oxides do not appear with apatite, but after these laminae until 13,810 μm cryptomelane was detected again. From 13,820 μm to 15,410 μm manganese oxide laminae were observed (manganite and cryptomelane), with traces of apatite. Until 16,040 μm 200–300 μm cycles of apatite and manganese oxide (manganite and cryptomelane) were discerned. From 16,050 μm to 16,980 μm apatite was identified. Between 16,330–16,340 μm uranyl sulphate lamina was seen with traces of apatite. Until the end of of the section, the apatite layer cyclically contains 10–20 μm thick manganese oxide laminae (manjiroite, romanéchite (psilomelane)) and feldspar, and 10–50 μm thick cycles of organic material (types graphite and org 1). Quartz occurs at 13,630 μm (very frequent), 13,650 μm (frequent), and at 18,000 μm. Rhodochrosite occurs at 16,370 μm (high amount).

5. Discussion

A complex investigation of samples was carried out, resulting in a large set of data. In accordance with the previous data, a volcanic-pyroclastic hydrothermal system can be proposed as the host rock of the P-Mn-U-Be-HREE-enrichment in phosphorite bodies (Csáki and Csáki, 1973; Kubovics et al., 1989; Polgári et al., 2000; Szabó and Vincze, 2013; Zajzon et al., 2014). The question is how the indication was formed in such a host rock, which is commonly widespread all over the world without any similar enrichments.

To answer this basic question, we used a complex interpretation of data in a multi- disciplinary approach. We took the following aspects into consideration: geological, petrological, and tectonic settings, micro-texture, embedded micro-mineralogy, chemical composition of minerals (major and trace elements) and organic matter, syngenetic and diagenetic processes. The previous and most appropriate formation model is a hydrothermal vent precipitation deposited in a marine, volcanoclastic environment accumulating elements (Be, U, REE, etc.) into the apatite structure (Szabó and Vincze, 2013; Zajzon et al., 2014). Preserving some main aspects of this previous model (“a hydrothermal vent precipitation deposited in a marine, volcanoclastic environment”), for element enrichment we propose a novel and complex interpretation as discussed below.

5.1. Biogenicity

In all of the thin sections, the high resolution optical rock microscopy (100-1000x) depicts series of biomat microstructures as main constituents (Fig. 7a-h), where some representative parts are indicated by arrows in the respective photos; it is obvious that this microbial micro-texture (mineralized biosignatures) is a basic syngenetic feature of all the samples. These microbially mediated characteristics are also visible in the host rocks (stromatolitic structures). These micro-textures are filamentous, inner necklace-like, or coccoid forms and aggregates, vermiform brain-like micro-texture, and the whole sample has a densely woven fabric. The thin sections represent mineralized biomats and other biosignatures (cyanobacteria) and also the mineralized phases of cell and EPS material (green clays, apatite, feldspar, tourmaline, segregated quartz, etc.) based on micro-textural observations (also Figs. 5–8). These micro-textural results turned our attention to microbially mediated mineralizations and element enrichments. Mineralized microbially mediated systems represent a unique type among ore mineral formation.

In situ measurements (FTIR and Raman spectroscopy), yielded

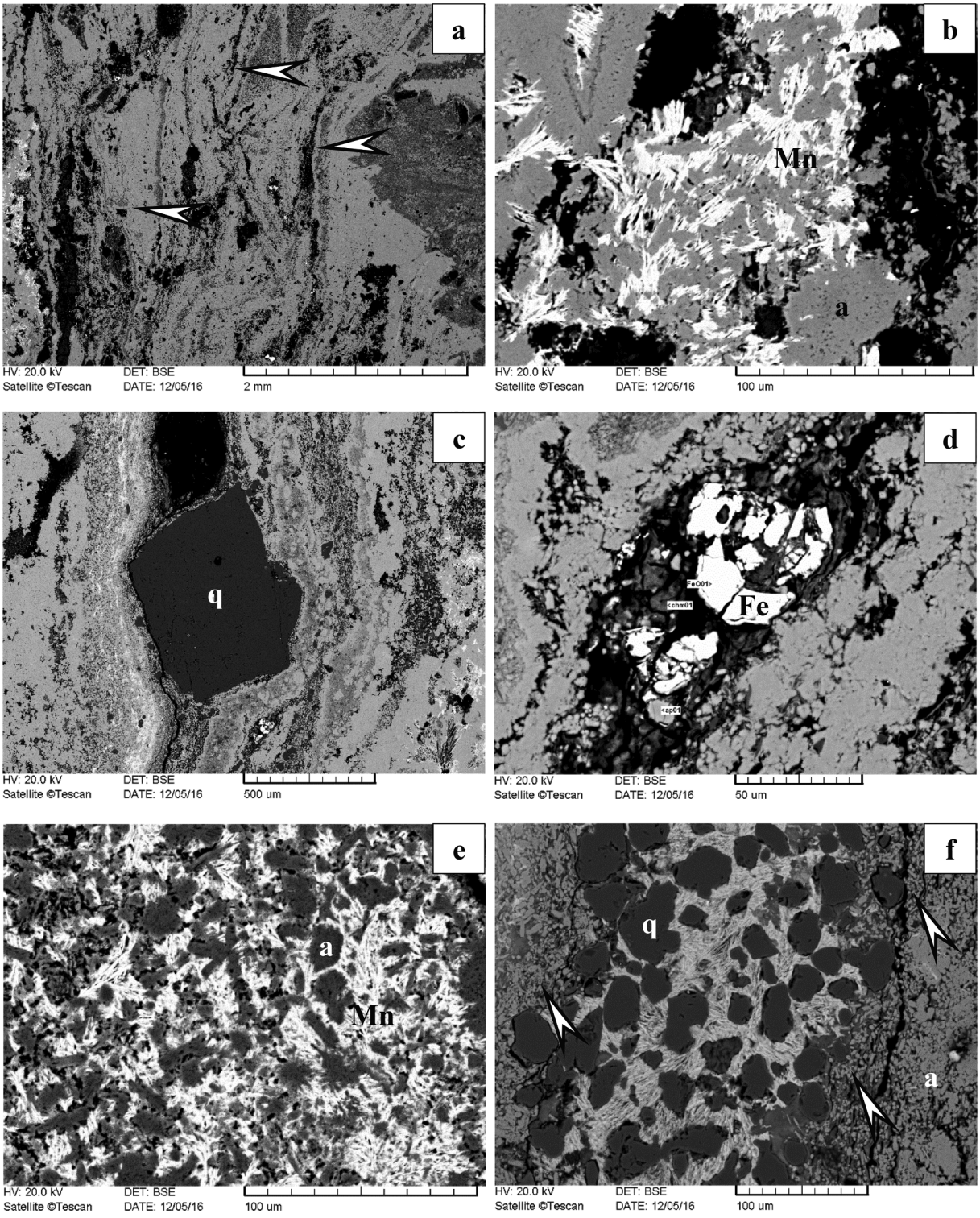

Fig. 10. SEM-EDS photos of the samples (back scattered electron images). Mineralogical distribution, sample Bszk-1 (SEM-EDS). (a) Folded apatite biomat with Mn oxide (arrow); (b) needle-like Mn oxide (light phase) and apatite (gray); (c) huge angular quartzite grain displacing woven apatite-bearing biomat and Mn oxide (light phase); (d) goethite after globular pyrite in fluffy fine-grained apatite; (e) needle-like fibrous Mn oxide (light phase) and apatite; (f) quartz grains cemented by needle-like fibrous Mn oxide and small coccoid-like apatite patches (arrows) around them.

"bioindicator" minerals (braunite, manjiroite, rhodochrosite, ferrihydrite, goethite, hematite, albite, quartz, apatite, montmorillonite) such as those reported by other studies (Skinner, 1993; Fortin et al., 1997; Konhauser, 1998; Ehrlich, 2002; Knoll et al., 2012). The presence of variable organic matter constituents occurring in the microbial-like textures as remnants of earlier microbial activity supports our scenario.

5.2. Metallogenesis

Mineral assemblage and paragenesis is given in Table 5. Diagenetic mineralization of the microbially mediated system is responsible for the unique mineral assemblage and element enrichment, with P in the focus, in accordance with Dill (2010). Element enrichments in ore

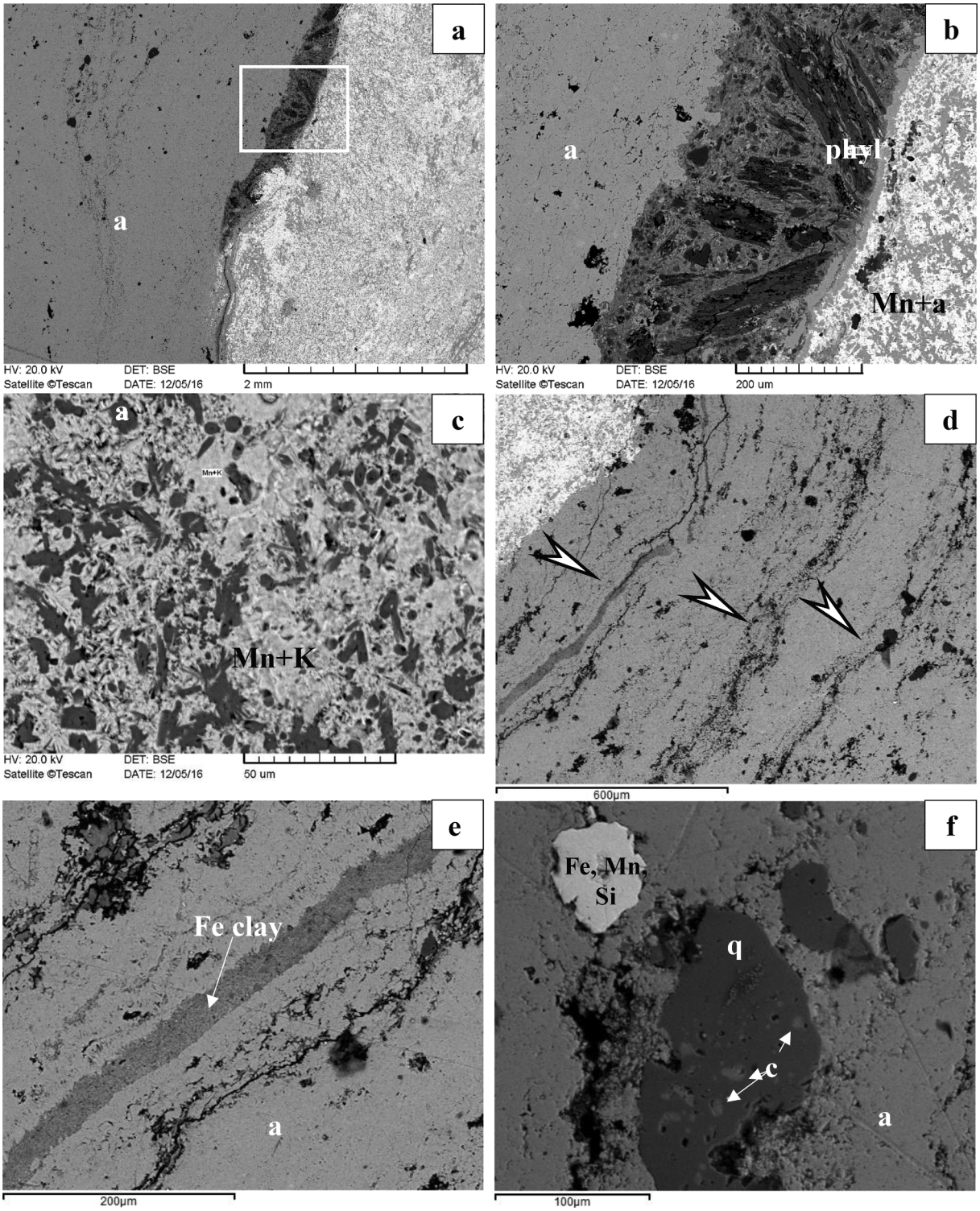

Fig. 11. SEM-EDS photos of the samples (back scattered electron images). Mineralogical distribution, sample Bszk-1 (SEM-EDS). (a) Apatite (dark phase) and Mn oxide-apatite mixture separated by mica-rich phase; (b) phyllosilicate-bearing rock fragments in apatite with Mn oxide-rich right marginal part, higher magnification of (a); (c) apatite (better crystallized grains) and patches with Mn oxide (back scattered electron images – BEI; Eötvös University, Budapest); (d) Biofilm series (arrows) in apatite host, the light phase is Mn, K-bearing; (e) Fe-bearing clay in biofilm; (f) Calcite inclusions in quartz.

minerals form discrete minerals or they bind to phosphorite, Mn-oxide, etc.

Be-ores generally relate to felsic magmatic or volcanic-pyroclastic-hydrothermal processes (Levinson, 1962). U, Mn, Zn, Li, and REEs also occur in such conditions (Varnavas and Papavasiliou, 2020). However, U is also typical for a sedimentary environment, together with Mn and Fe (Lovley, 1991). Phosphorous is a common constituent in marine conditions, where microbially mediated apatite (phosphorite) formations occur (Crosby and Bailey, 2012).

Microbially mediated processes basically contributed most of the enriched elements of the indication. The enrichment factor was microbial mediation. The separation effect, where the separation of

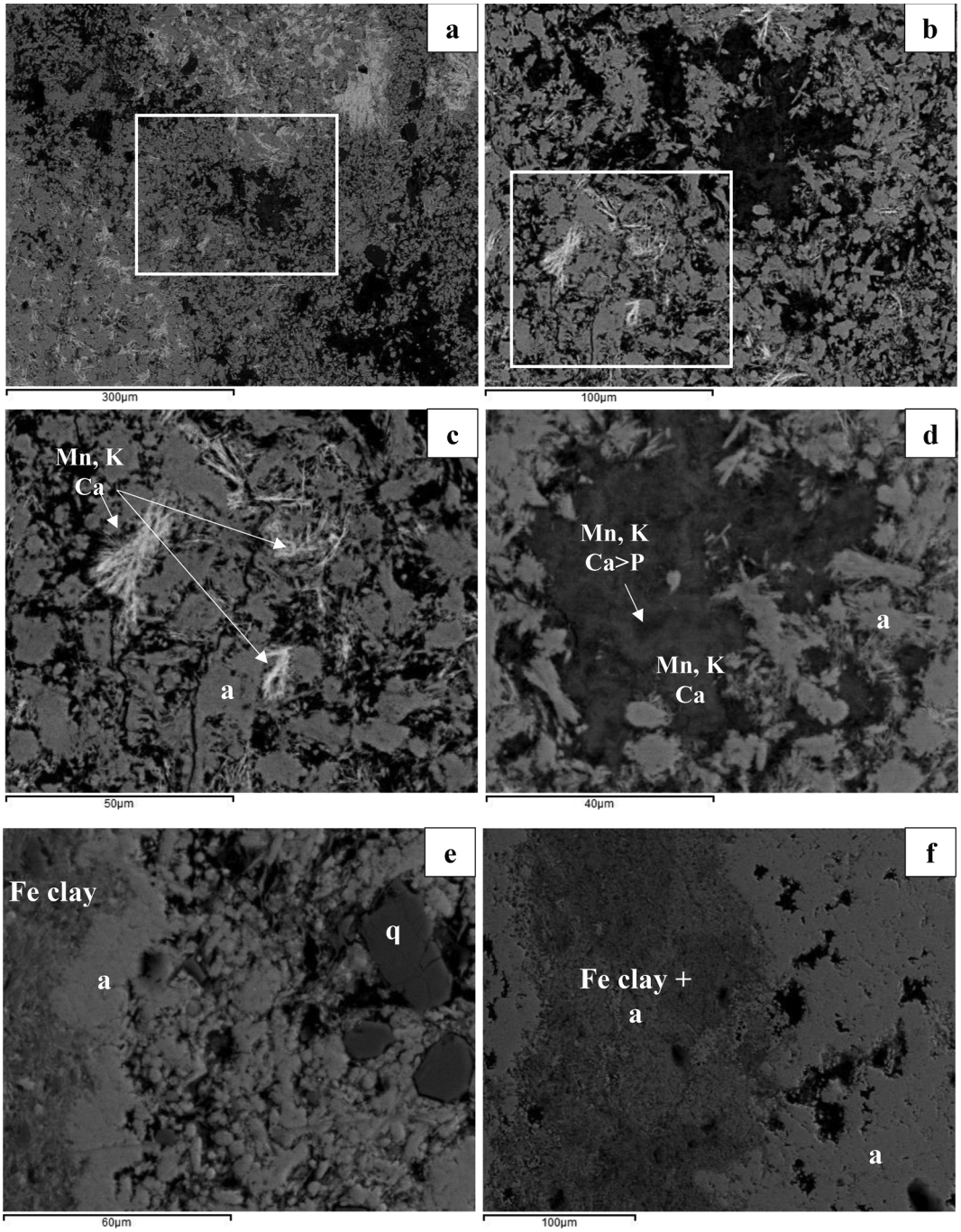

Fig. 12. SEM-EDS photos of the samples (back scattered electron images). Mineralogical distribution, sample Bszk-1 (SEM-EDS). (a) Distribution of elements on micrometer scale; (b) higher magnification of (a); (c) fine, needle-like fibrous Mn-, K-, Ca-bearing phases in apatite host, higher magnification of (b); (d) Poorly mineralized Mn-, K-, Ca-, P-bearing and Mn-, K-, Ca-bearing phases in apatite host, the apatite shows fine, needle-like fibrous texture, higher magnification of (a); (e) Fluffy and compact apatite and Fe-bearing clay with quartz particles; (f) very fine-grained apatite and Fe-bearing clay mixture in fine-grained but "massive" apatite host (back scattered electron images – BEI; IGGR, Budapest). Legend: q - quartz; Mn - Mn oxide; Mn + K - K-bearing Mn oxide; Mn, K, Ca-K- and Ca-bearing Mn oxide; Fe - Fe oxide; phyl - phyllosilicate; a - apatite. c - calcite; Fe clay - Fe-bearing clay; Mn, K, Ca > P - Mn-K-Ca-bearing phase with P traces; Fe, Mn, Si - Fe-,Mn-, Si-bearing particle.

microbial activity occurred by tuff contribution, interrupted the highly effective recycling of P by microbes. This is one of the main factors of P enrichment in nature. Tuff contribution is clearly visible under the microscope. Synsediment brecciation, broken biomats, and also local broken tuff parts are visible (Figs. 5–8). At some parts coarser, 100–500 µm large weathered minerals (e.g., quartz, and also rock fragments) can be seen, which fell onto the surface of the biofilms (altered pumices?; Fig. 6e). Remnants of fine-grained tuff containing remnants of volcanic glass (bone-like shape structures) also occur. The REE element composition and distribution is very similar in the indication and the host rock, which supports a similar source and mode of formation (Polgári et al., 2018).

5.3. Diagenetic processes and paleoenvironment

In contrast to earlier investigations, we found a great deal of evidence for a syngenetic origin via rock petrography. The micro-laminated texture often shows signs of synsedimentary sliding or faulting

Table 2
Bulk mineralogy (XRD).

Mineral	Bszk-1a	Bszk-1b	Bszk-2	Bszk-3	Bszk-4	Bszk-5a	Bszk-5b	Bszk-5c	Bszk-6	Bszk-7	Bszk-8–1
apatite	**	**	***	***	*	**	***	*	–	–	*
feldspar	**	**	*	–	–	–	–	–	–	–	–
quartz	**	*	–	**	***	***	*	***	–	–	***
mica	min	min	–	–	–	–	–	–	–	–	–
smectite	–	–	–	–	–	–	*	–	–	–	–
birnessite/hollandite	*	–	–	*	–	–	min	–	*	*	–
todorokite	–	–	min	–	–	–	min	–	*	*	–
ramsdellite	–	–	–	–	–	–	–	–	**	**	–
pyrolusite	–	–	–	–	–	–	–	–	**	**	–

Legend: *** major; ** moderate; * low; min rare; - not detected.

processes. The larger grains of the volcanic environment (porphyroclasts, pumices, lithic clasts) reflect plastic behaviour of the incorporating band. Diagenetic processes deeply overprinted the original picture, both in mineralogy and micro-texture. Mineralization of cell and EPS material and its effects (released ions like Si, K, Na, Ca, Mg, etc.) result in a mineral assemblage which is difficult to interpret, because some diagenetic minerals are also typical volcanic minerals (quartz, feldspar, tourmaline; Polgári et al., 1991, 2019; Ostwald and Bolton, 1990; Schwertmann and Cornell, 2007; Rajabzadeh et al., 2017). Microbially mediated processes, the role of cell metabolism and extracellular polymeric substances, are very important in syngenetic mineralization. They also represent a considerable element source pool, as they bond cations and anions, which release via diagenesis. These are very effective factors influencing syn- and diagenetic mineralization processes. To distinguish the two basically different formations (volcanic and diagenetic-sedimentary), CL is a good tool, because the volcanic originated minerals show luminescence, while the diagenetic ones do not (Marshall, 1998). This also helped with clarification of debris origin. The diagenetic quartz exhibits a characteristic microstructure, which refers to specific types of fluid flow during crystal growth. Quartz grains often contain numerous small calcite inclusions of μm size. Furthermore, we found albite grains with the same calcite inclusions, as well as quartz and albite grains containing cryptocrystalline apatite inclusions – Similar to the most characteristic apatite of the apatite-rich bands. These new features show that these grains are likely to have formed slightly later than the apatite. The quartz-albite-mica-rich layers probably had a tufaceous origin, where glass-rich components diagenetically crystallized to quartz, albite, and mica.

Phosphatization was an important process in eliminating earlier pumice and volcanic glass particles, and also formed better crystallized apatite.

Tourmaline is also characteristic for the border zone between the brecciated clasts of the siliceous rock and the phosphorite. The mica-tourmaline-pyrite association seems to substitute the quartzine-rich material. The quartzine is probably secondary mineral, from the hydrothermally active period. Around and inside the tourmaline, mineralized microbial biosignatures occur (Fig. 7f, 8g and h). Diagenetic tourmaline has also been reported from other occurrences (Henry and Dutrow, 2012). Under diagenetic conditions, tourmaline can develop as new, authigenic crystals, which are found in many sedimentary or weakly metamorphosed meta-sedimentary rocks as well as fluid-dominated geothermal systems. It appears to be diagnostic for an oxidizing and low temperature environment with high Na in the fluid, which supports our results. Similarly, high Na in the fluids formed on cell and EPS decomposition supported aegirine formation in a Neoproterozoic Mn ore at Urucum (Biondi et al., 2020). Potassium enrichment in a potassic metasomatized andesite formation (hydrothermally weathered Fe-rich occurrences) in the Mátra Mts. of Hungary (Varga, 1992; Nagy, 2006) may be a similar source and formation process.

Looking at the chemical formula of tourmaline, it is clear that it can also be responsible for some element enrichments (Li, Be, V, Cr, Ti, Cu, Mg, etc.). Albitization of feldspar – Na incorporation (substitution) – as metasomatism-like and/or metamorphic effects can occur in the frame of organic matter decomposition (Polgári et al., 2019). Green clays (smectite, celadonite) appear in the vicinity of the mineralized biosignatures, which are common constituents in microbially mediated environments (Polgári et al., 2012a, 2012b; Gyollai et al., 2014, 2015, 2017).

In time, the first brecciation event is thought to be close to the formation of the phosphorite, because the apatite and Mn-oxide cementation of brecciated clasts contain the same signs of microbial activity (filamentous, necklace-like, coccoidal forms, aggregates in apatite and reddish brown concentric forms in Mn-oxide). However, this event also stopped the microbial activity, because apatite-rich bands do not exist apart from the brecciated parts.

The occurrence of microbially mediated Fe-oxide together with Mn-enrichment and clay minerals (montmorillonite) and also tourmaline focus on suboxic-oxic and semi-neutral slightly basic conditions during syngenetic and early diagenetic processes under low-moderate T conditions.

5.4. Character of element enrichments

From the recent and earlier published results a multiphase formation model was elaborated based on a complex dataset from geology, petrology, macro- and micro-texture, bulk and *in situ* mineralogy and also the distribution of variable embedded organic matter and geochemical features (main and trace elements, also REE). The genetic draft supports post-volcanic exhalative-hydrothermal activity as an element source, but it does not explain the element enrichment. The geochemical character of each element, such as U or the entire group containing U, Be, REE, Mn, and P is very different and needs a detailed interpretation. In the case of P, but also in the case of Mn, Fe, U, As, and Zn, microbially mediated processes immediately appear as possible enrichment factors (Polgári, 2016). The published element correlations are also very peculiar, with positive correlation of U-P, Be-P and REE-P (Szabó and Vincze, 2013). Among the minerals of the ore indication several “bioindicator” minerals occur (Skinner, 1993), like Ca-phosphate (apatite), Mn-oxide, Fe-phosphate (dufrénite), Fe-oxyhydroxide (ferrihydrite), and pyrite, and the U minerals also belong to this group.

Numerous publications report on the biogeochemical behaviour of elements, the metabolic diversity of chemolithoautotrophic bacteria, and the development of methodology permitting the study of the connection of metabolism and biomineralization on the nanoscale (e.g., Ehrlich, 2002; Wackett et al., 2004; Knoll et al., 2012). Recent analogies and experiments prove the basic role of microbial activity and mediation concerning the enrichment of elements in the solid phase. The metabolic processes take place according to regularity, and the different processes influence each other on an optimum condition along the minimum level of energy. The result of a complex microbial mediation in the geological sense can be a huge rock body and also mineral deposits (Polgári et al., 2012b, 2019; Southam and Sanders, 2005; etc.).

Table 3
Mineral and organic matter composition, distribution and frequency of samples by FTIR.

Mineral phase	References	Sample ID	Bszk-1								Bszk-2				Bszk-3					Bszk-4						Bszk-5			
		Measuring area	1	2	3	4	5	6	7	8	1	2	3	4	l	2	3	4	5	1	2	3	4	5	6	1	2	3	4
		Total No. of spectra→	8	9	7	17	13	14	10	3	7	8	4	7	4	4	6	5	6	3	9	7	6	4	6	5	4	7	5
		Wavelength [cm^{-1}]																											
Beryllonite $NaBePO_4$	RRUFF	680, 722, 770; 1043 s 1011sh, 1083sh, 1139sh	0	0	0	0	0		0	0	**7**	0	0	0	0	0	0	0	0	**1**	0	0	0	**1**	0	0	0	0	0
Apatite $[(Ca_{10}(PO_4)_6(OH, F, Cl)_2]$	Beasley et al. (2014)	790, 1012, 1093	0	0	**3**	0	**13**	**3**	**6**	0		**6**	0	0	**2**	**4**	**5**	**1**	**2**	0	**5**	0	**5**	0	0	**2**	0	**1**	0
Whewellite $Ca(C_2O_4)\ H_2O$	RRUFF	669, 780, 1306 s. 1605 s	0	0	0	0	0		0	0	**7**	0	0	0	0	0	0	**5**	**2**	0	0	0	0	0	0	0	0	**4**	0
Feldspar $NaAlSi_3O_8$	Müller et al. (2014)	798, 950, 1000	**4**	**5**	**3**	**11**	**1**	**3**	0	0	0	**1**	0	0	0	0	0	0	**4**	**1**	0	0	0	0	0	0	0	0	0
Duphrènite $Fe^{2+}Fe_4^{3+}(PO_4)_3(OH)_5{\cdot}2(H_2O)$	Frost et al. (2013)	995 s (1030, 1070 1135)	**4**	**4**	0	0	0	0	**4**	0	0	0	**3**	0	0	0	0	**2**	**1**	0	0	0	0	**3**	**4**	**3**	**2**	0	**5**
Ferrihydrite FeOOH	Glotch & Rossman (2009)	692, 878, 3400	0	0	0	0	**12**	**8**	**5**	**3**	0	0	0	0	0	0	**1**	**2**	0	0	**3**	0	**1**	0	0	0	**2**	**6**	0
Tourmaline $(Na,Ca)(Mg,Li,Al,Fe^{2+},Fe^{3+})_3(Al,Mg)_6(BO_3)_3Si_6O_{18}(OH,O,F)_4$	RRUFF	960, 1028sh, 1243, 1350sh	0	0	0	0	0	0	0	0	0	0	0	0	**2**	0	0	0	0	0	**3**	0	0	0	**2**	0	0	0	0
Hematite Fe_2O_3	Glotch & Rossman (2009)	600, 1019	0	0	**1**	**2**	**12**	0	0	3	0	1	0	0	0	0	0	0	**1**	**1**	0	0	0	0	0	0	0	**6**	0
Goethite FeOOH	Glotch and Rossman (2009)	798, 910	0	0	0	**4**	0	0	0	0	0	0	0	0	0	0	0	0	0	0	0	0	0	0	0	0	0	0	0
Berhierite $FeSb_2S_4$	RRUFF	1135 broad	0	0	0	0	0	0	0	0	0	0	0	0	0	0	**1**	0	0	0	0	0	0	0	0	0	0	0	0
Montmorillonite $(Na,Ca)_{0.33}(Al,Mg)_2(Si_4O_{10})(OH)_2{\cdot}nH_2O$	Madejová & Komádel (2001)	989, 1000, 3570	0	0	0	0	**13**	0	0	0	0	0	0	0	0	0	0	0	**2**	0	0	0	0	0	0	0	0	0	0
Quartz SiO_2	Müller et al. (2014)	701, 776, 1059	0		0	0	0	0	0	0	0	0	**1**	**7**	0	0	0	**1**	**2**	0	0	0	0	0	0	0	0	0	0
Organic matter																													
v C = C/C-O	Parikh & Chorover (2006)	1070–1240	**8**	**9**	**4**	**10**	0	**6**	**6**	**4**	**7**	**7**	0	0	0	**2**	**5**	**4**	**6**	0	**5**	**6**	**4**	0	0	**5**	**2**	**7**	0
vs CO	Parikh & Chorover (2006)	1360–1450	**8**	**9**	**4**	**10**	**0**	**6**	**6**	**4**	**7**	**7**	**4**	0	**4**	**2**	**5**	**4**	**6**	0	**5**	**6**	**4**	0	0	**5**	**2**	**7**	0
d CH2	Parikh & Chorover (2006)	1454–1482	**8**	**9**	**4**	**10**	**13**	**14**	**6**	**4**	**7**	**1**	**4**	**3**	**4**	**4**	**6**	**3**	**6**	0	**5**	**6**	**4**	**4**	**6**	**5**	**2**	**7**	**5**
C-N, CH deformation	Parikh & Chorover (2006)	1526	0	0	0	0	0	**8**	0	**4**	**7**	**7**	0	**3**	**2**	**2**	**5**	**5**	**2**	0	**7**	**7**	**6**	0	**4**	**5**	0	**7**	0
C-N N–H amide II	Parikh & Chorover (2006)	1540–1550	0	0	0	0	0	**8**	**10**	0	**7**	**7**	0	0	**2**	**2**	**5**	**5**	**2**	0	**7**	**7**	**6**	0	**4**	**5**	0	**7**	0
C = C asym. Stretch	Parikh & Chorover (2006)	1598	0	0	0	0	0	0	0	0	**7**	0	0	0	0	0	0	0	**4**	0	**7**	**7**	0	0	**4**	**5**	0	0	0
amide I C = O, C-N, N_H	Parikh & Chorover (2006)	1632–1652	0	0	0	0	0	0	0	0	**7**	**7**	0	0	**2**	**2**	**5**	**5**	**2**	0	**7**	**7**	**6**	0	0	0	0	**7**	0
v as COOH	Parikh & Chorover (2006)	1720–29	0	0	0	0	0	0	0	0	**7**	**7**	0	0	**2**	0	0	0	**4**	0	0	0	0	**4**	**6**	0	**4**	**7**	0
C-O	Parikh & Chorover (2006)	1799	0	0	0	0	0	0	0	**7**	**7**	**7**	0	0	0	0	0	0	0	0	0	0	**6**	0	0	**5**	0	**7**	**5**
CO	Müller et al. (2014)	2343	**8**	**9**	**7**	**17**	**13**	**14**	0	**7**	**7**	**8**	**4**	**7**	**4**	**4**	0	**5**	**6**	**3**	**9**	**7**	**6**	**4**	**6**	**5**	**4**	**7**	**5**
CO	Müller et al. (2014)	2365	**8**	**9**	**7**	**17**	**13**	**14**	0	0	**7**	**8**	**4**	**7**	**4**	**4**	0	**5**	**6**	**3**	**9**	**7**	0	**4**	**6**	**5**	**4**	**7**	**5**
C–H sym. Stretch CH2	Parikh & Chorover (2006)	2853	0	0	0	0	0	0	0	0	**7**	**8**	**4**	**7**	**4**	**4**	**6**	**5**	**6**	**3**	0	0	0	0	0	**5**	**4**	**7**	**5**
C–H asym. Stretch CH2	Parikh & Chorover (2006)	2926	0	0	0	0	0	0	0	0	**7**	**8**	**4**	**7**	**4**	**4**	**6**	**5**	**6**	**3**	0	0	0	0	0	**5**	**4**	**7**	**5**
OH	Madejová & Komádel (2001)	3230–3700	**8**	**9**	0	0	0	**14**	0	0	**7**	0	0	0	0	0	0	**5**	**2**	0	0	0	0	0	0	0	0	0	0

Table 4
Raman vibration of minerals and detected types of organic materials.

Minerals[ref]	Bands		Sect1	Sect2	Sect3	Sect4
manjiroite[1]	641s		8	59	17	12
manganite[2]	387, 528, 537, 621		322	54	3	202
cryptomelane[2]	183s, 280, 511, 581s, 637		367	126	17	223
romanéchite[3]	284, 372, 515, 578s, 643s, 721		84	108	68	40
pyrolusite[2]	219w, 291w, 404w, 533s, 655s, 756w		9	11	0	0
birnessite[3]	296, 303, 506, 575, 656, 730		6	4	0	1
braunite[1]	210s 331, 376w, 510m, 622, 685		6	1	0	0
rodochrosite[1]	181, 287, 721, 1087		0	6	0	1
hematite[4]	222, 290, 408, 490, 607 hem		3	2	0	0
ferryhydrite[4]	361, 508, 707, w, 1045s		1	3	0	1
goethite[4]	162, 243, 297s, 385s, 477 545		8	3	6	1
lepidocrocite[4]	140, 214w, 284s, 297, 345, 374w, 524m		1	1	11	0
apatite[1]	427, 587, 605 w, 965s, 1040 w, 1078 w		55	317	441	225
albite[1]	478s, 507s, 287m, 330, 244w, 207sh, 182m, 161 sh		41	60	41	43
quartz[1]	125, 207, 353, 393 w, 464s		2	4	1	3
montmorillonite[1]	186, 360, 681		2	1	1	0
johannite (uranyl sulphate)[5]	785s		0	0	0	6
Types of organic matter[6,7,8,9]		Organic matter				
org 1	824, 1186, 1608	aromatic CH bending, aliphatic CH stretching, fluerene	14	10	7	14
graphite[8]	1599	graphite	96	60	25	34
org 2	825, 1109, 1186, 1607	aromatic CH bending, aliphatic CH stretching, fluerene	2	3	1	2
org 3	824, 1186, 1345, 1608	aromatic CH bending, aliphatic CH stretching, CH3, fluerene	3	2	2	0
org 4	825, 1109, 1186, 1386 1607	aromatic CH bending, aliphatic CH stretching, fluerene	4	4	0	0
org 5	1567, 1742	quadrant CH stretching in cylic aromatic ring system, carboxyls	1	2	2	0
org 6	825, 1109, 1186, 1386, 1469, 1607	aromatic CH bending, aliphatic CH stretching, CH3, CH2/CH3, fluerene	1	3	0	2
org 7	762, 816, 1096, 1186, 1350, 1618	CH out of plane vibration, aromatic CH bending, aliphatic CH stretching, fluerene	1	0	1	0
org 8	1186, 1573	aliphatic CH stretching, quadrant CH stretching modes of cyclic aromatic ring	10	11	0	2
org 9	825, 1608, 1757	aromatic CH bending, fluerene, carboxyls	1	0	4	0
org 10	825, 1109, 1186, 1386, 1469, 1527, 1607	aromatic CH bending, aliphatic CH stretching, CH3, C=C strertching in polyenes, fluerene	7	0	1	2
org 11	1330, 1580	CH3, quadrant stretching of CH of aromatic ring	1	21	2	12
org 12	825, 1095, 1386, 1591, 1770	aromatic CH bending, C–H in plane bendig, CH3, quadrant CH stretching of cyclic aromatic ring system, carboxyls	0	2	0	0
org 13	1186, 1464, 1527	aliphatic CH stretching, CH2/CH3, C=C stretching of polyenes	0	3	0	6
org 14	1330, 1580, 1757	CH3, quadrant CH stretching modes in aromatic ring system, carboxyls	0	0	1	4

450 spectra were taken in each sections (Fig. 13), the step is 10 μm. The number of spectra of detected minerals are summarized in column sections (sect) 1–4. References: 1 – RRUFF; 21 – Sepúlveda et al. (2015); 31 – Julien et al. (2004); 41 – Das & Hendry (2011); 51 – Frost et al. (2005); 61 – Jehlička et al. (2009); 71 – Okolo et al. (2015); 81 – Chen et al. (2007); 91 – Orange et al. (1996).

5.5. Source of elements mineralized feeder and mound zone: Mineralogy, micro-texture and paleoenvironmental considerations

The source of elements was hydrothermal – The mineralized micro-texture together with mineralized microbially mediated forms built up by Fe-oxide minerals support this scenario and fit well with previous conclusions (Polgári et al., 2012a,b; Gyollai et al., 2015; Yu et al., 2019).

Beryllium has a microbial connection. The similar behaviour of $BeF_3{*}H_2O$ to phosphate can positively or negatively affect the numerous enzymatic and regulating phosphatase functions. Fluoride and biofilms have community interactions in the vicinity of weak organic acidic producing biofilms (Marquis et al., 2003). It is known that metal Be suffers from microbial corrosion unless defended by a protective coating (Vaidya et al., 1999). Further, in the case of some bacteria Be enrichment was detected in their outer membrane (Robles and Aller, 1994).

In general, beryllium forms very stable inert metallo-organic complexes with hydroxylated organic compounds. Because most coals have some beryllium in their organic compounds, and some have quite large amounts, it is possible that plant adsorption and formation of complexes are responsible for the beryllium enrichment in coal (Stadnichenko et al., 1961).

Epithermal beryllium deposits (where BeO content is less than 1 wt %, in beryl – $Be_3Al_2(SiO3)_6$ and bertrandite – $Be_4Si_2O_7(OH)_2$) in western Utah at the Spor Mountains and Honeycomb Hills are uniquely associated with rhyolite of Late Tertiary age and are restricted to porous water-laid tuff and breccia that contain carbonate clasts, similarly to the Bükkszentkereszt indication. A shallow epithermal environment is favourable for deposition of Be in the form of silicates. Also, the Be deposits are near both local and regional faults, which probably provided conduits for mineralizing fluids. The enriched elements are also similar to our case, containing fluorite, lithium (in smectite), manganese oxides, Zn (in smectite and Mn-oxides), and U, as well as many trace elements (F, Cs, Li, Ga, Nb, Y, etc.). However, due to the enrichment of P, the missing or scarce micrometer-scale occurrence of individual Be minerals (beryllonite-$NaBePO_4$), and the rare mineral occurrence of U (scarce johannite), the type of enrichment is basically different (Lindsey, 1977). At Bükkszentkereszt, Na-bearing Be-phosphate occurs, in harmony with the mineral assemblage.

Uranium in solution occurs as U(VI) in the form of a uranyl-carbonate complex and can be enriched in solid form, if it is reduced to U(IV). The (IV) and (VI) valencies are interchangeable in nature, so the dissolution and precipitation of U follow each other. This is supported by the fact that carbonate ions can easily lead to the dissolution of U. Microbial U(VI) reduction is inhibited by Ca (Brooks et al., 2003). Numerous autotrophic and heterotrophic microbes are able to dissolve U or produce oxidative/reductive chemical compounds which precipitate this element. These processes can be direct or indirect. In the indirect case it happens through the mediation of other metal/microbe redox processes. Fe(III) and Mn(IV) ions are among the most effective oxidants in nature which mobilise U (Ehrlich, 2002).

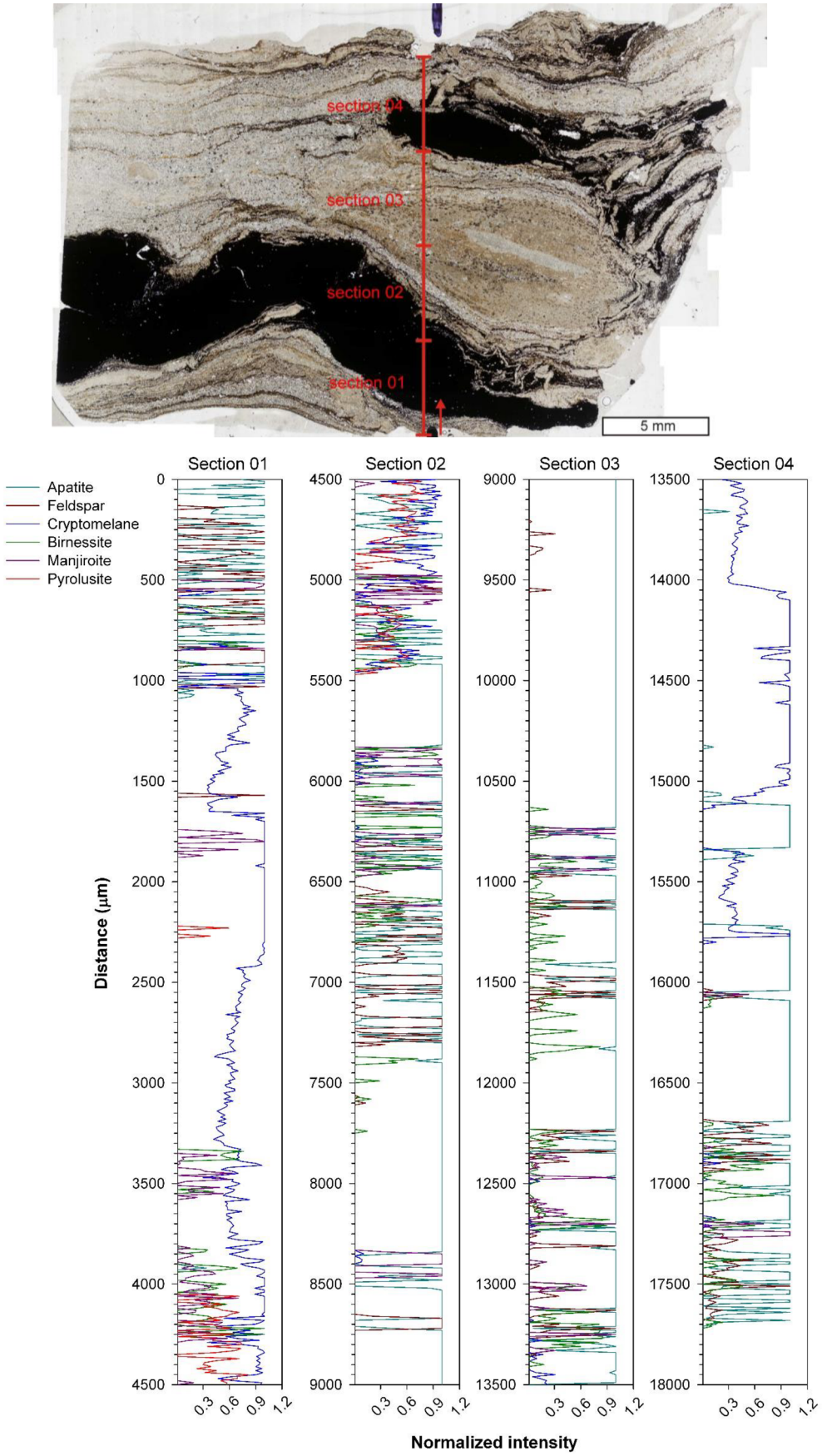

Fig. 13. Raman spectroscopy line measurements along the profile on the sample (sample Bszk-1).

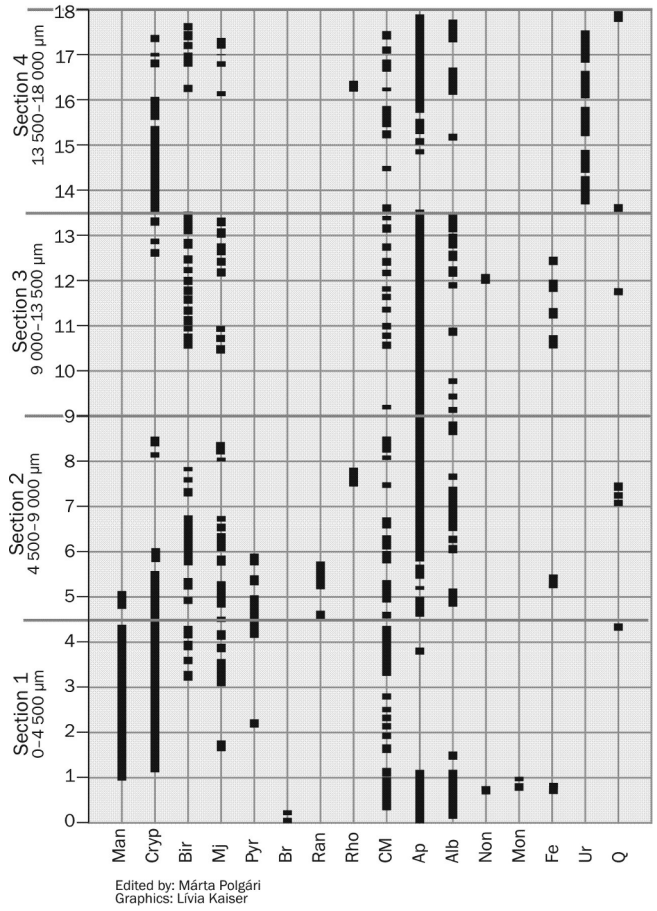

Fig. 14. Frequency of minerals along Raman sections. Legend: Man - manganite; Cryp - cryptomelane; Bir - birnessite; Mj - manjiroite; Pyr - pyrolusite; Br - braunite; Ran - ranciéite; Rho - rhodochrosite; CM; variable organic matter; Ap - apatite; Alb - albite; Non - nontronite; Mon - montmorillonite; Fe - Fe oxides (goethite, hematite, ferrihydrite, lepidocrocite); Ur - johannite; Q - quartz.

Uranium is important bioessential element, could be mobilized and fixated by fungi together with molybdenum (Berthelin and Munier-Lamy, 1983). Vanadium and uranium can also be utilized in bacterial respiration, and for algal growth: Geobacter and Shewanella are able to use U along with the metals Fe(III), Co(III), Cr(VI), and Mn(IV) as a terminal electron acceptor in cellular respiration (Park et al., 2016).

According to syn- and diagenetic processes, the reaction between pyrite forming via sulphate reduction and Mn-oxide formed via enzymatic Mn oxidation produces Fe(III), which is able to oxidize and dissolve U. Pracejus et al. (1988) propose an easier way of Fe(III) formation, where Fe(II) reservoir is in solution or adsorbed on clay minerals, to start the redox reaction with MnO_2. The dissolved U precipitates and accumulates first probably by adsorption on organic matter via reducing microbial processes. During this, Fe turns to (II) valence form and precipitates as pyrite. These processes follow each other in a cyclic way.

The effect of Mn-oxides was detected via microbial processes in reduction of U(VI) and enrichment in solid phase (Fredrickson et al., 2002). The solid phase forms in the case of Mn being present as oxide (Mn^{4+}), while U is the reduced phase (U^{4+}). In the excess of Mn-oxide, the initial U(VI) was microbially reduced, which supports the direct utility of U by bacteria for their metabolism (Abdelouas et al., 1998). The U(IV) enrichment in the periplasma of cell can remain physically protected from later oxidative processes, which can result in an extended redox inequality status.

Sulphate reducing bacteria can also interact with Cr(VI), Mn (IV), Fe (III), and U(VI) ions serving as electron acceptors (Lovly, 1993; Lovly et al., 1993; Tebo and Obraztsova, 1998). In the case of REEs, similar processes were reported by Texier et al., (2000). In a recent study, we report the presence of johannite - $Cu[UO_2(OH)SO_4]_2{\cdot}8H_2O$ a U-sulfate, but the effect of Mn and Fe microbial cycles can also influence U enrichment, which supports our scenario (Biondi et al., 2020).

Rare Earth Elements (REE) can be enriched selectively also by direct microbial oxidation. Cerium oxidizes together with Mn via microbially mediated processes, in the frame of which specific oxidation ratio of Ce/Mn is constant in a wide range of the littoral and oceanic environments (Moffett, 1990, 1994; Moffett and Ho, 1996).

Phosphorus is an essential nutrient for life and is a central component of all biological systems. It is key to the formation of membranes, the transfer of genetic information, and the cycling and storage of energy. Recent marine phosphorites spatially correlate with the habitats of vacuolated sulfide-oxidizing bacteria that store polyphosphates under oxic conditions to be utilized under sulfidic conditions (Bailey et al., 2013). Hydrolysis of the stored polyphosphate results in the rapid precipitation of the phosphate-rich mineral apatite, providing a mechanism to explain the association between modern phosphorites and these bacteria. Modern sulfide-oxidizing bacteria that are partially encrusted in apatite provide evidence that bacterially mediated phosphogenesis can rapidly permineralize sulfide-oxidizing bacteria and perhaps other types of organic remains (Bailey et al., 2013).

The availability of P in nature is very limited as it occurs as insoluble Ca- or Fe-phosphate, or as an organic complex. Its concentration in the aqueous environment is much lower (0.01–0.07 mg/l) than the concentration of P in bacterial dried matter, which is around 1.5–2.5 wt %, an extremely high enrichment. In living organisms containing 1 wt% P, the enrichment is 140,000 times the Clark value. Because of the slow sedimentary P cycle, the biological community supplies the P demand by cyclization (recycling) with high speed recycling through the organic phase (Ehrlich, 2002; Knoll et al., 2012).

The role of microbial processes in the genesis of Jordanian Upper Cretaceous phosphorites was reported by Abed and Fakhouri (1990) in the form of granular and laminated phosphorites. These phosphorites are interpreted to have been deposited as algal mats in shallow, subtidal to intertidal environments similar to that of Bükkszentkereszt.

Detailed petrographic study of the Upper Cretaceous phosphatic chalks of northern France shows that phosphate occurs predominantly as phosphatized bacterial matter. Shiny phosphatic crusts on hardgrounds and anisotropic phosphate coatings on grains are interpreted as phosphate mineralized microbial ('micro-stromatolitic') structures. Phosphatic remains of ovoid bacteria and microbial colonies with botryoidal surfaces have been observed. The microbial community, which formed the crusts and grain coatings developed by surface accretion, whereas the other community grew solely in the intragranular porosity of grains and in the extragranular porosity of semilithified sediments. Analysis of these two types of microbial growth has also been documented from other phosphorite deposits (Lamboy, 1990).

Enrichment of P in geological environments generally occurs if the P-bearing material (dead organisms, fecal material, etc.) separates in space from the user organisms. The mineral shell that forms via the metabolism of chemolithotrophic bacteria can also hinder recycling. It is well known that the activity of the surficial phosphatizing enzyme of cells stimulates metal-phosphate formation, e.g., U enrichment (Macaskie et al., 1995; Fowle et al., 2000; Panak et al., 2002; Knopp et al., 2003; Suzuki and Banfield, 2004; Francis et al., 2004; Billon et al., 2004; Khijniak et al., 2005). Bioremediation and microbial dissolution experiments concerning U for mining and environmental protection purposes have been carried out (Elias et al., 2003; Landa, 2003; Schippers et al., 1995; Dwivedy and Mathur, 1995; Kalinowski et al. (2004)) and support our understanding of the processes.

Arsenic and Zinc are well-known bioessential elements; the microbial As cycle and the main role of Zn in enzymatic processes are important processes (Knoll et al., 2012).

Sb (antimony) influence enzyme activity of microbial growth (E. coli, B. subtilis and S. aureus) (An and Kim, 2009). The T. ferrooxidans

Table 5
Paragenetic sequence of minerals in Bükkszentkereszt area based on XRD, Raman and FTIR.

Table 5. Paragenetic sequence of minerals in Bükkszentkereszt area based on XRD, Raman and FTIR.					
Minerals/Processes	**Syngenesis**	**Diagenesis**	**Secondary**	**Method**	**Source/formation**
Mn mineral assemblage					
Oxides and hydroxide					
Pyrolusite ($Mn^{4+}O_2$)				XRD	This is an oxic phase, which can be formed (oxidation of Mn(II)) either by enzymatic processes if the conditions were obligatory oxic, or in this case more probably by active oxic surface catalysis on Fe-oxide and/or previously formed Mn-oxide (Morgan, 2005).
Cryptomelane ($KMn^{4+}{}_6Mn^{2+}{}_2O_{16}$)				XRD Raman	Cryptomelane is a reduced phase. K-analogue. This reduction can be interpreted by continuous Mn(II) infiltration, which reduces the previously formed Mn(IV)-oxide phase (this is very common)(Villalobos et al., 2003). Or, it can be interpreted by microbially mediated Mn(IV) reduction via organic matter decomposition, and in this sense the pyrochroite can be a transitional product between hollandite and the end phase rhodochrosite.
Manganite ($Mn^{3+}OOH$)				XRD Raman	Manganite is a reduced phase. This reduction can be interpreted by the continuous Mn(II) infiltration, which reduces the previously formed Mn(IV)-oxide phase (this is very common) (Villalobos et al., 2003).
Romanéchite (psilomelane) [$(Ba,H_2O,Mn_5O_{10}$, $Ba(Mn^{4+}, Mn^{3+})O_{10}.1.4H_2O)$]				XRD, Raman	Ba-analogue.
Ranciéite [$(Mn^{2+},Ca)Mn^{4+}{}_4O_9.3H_2O$]				XRD	Ranciéite is a reduced phase. This reduction can be interpreted by continuous Mn(II) infiltration, which reduces the previously formed Mn(IV)-oxide phase (this is very common)(Villalobos et al., 2003). Or, it can be interpreted by the microbially mediated Mn(IV) reduction via organic matter decomposition, and in this sense the pyrochroite can be a transitional product between hollandite and the end phase rhodochrosite.
Birnessite [$(Na,Ca)_{0.5}(Mn^{4+},Mn^{3+})_2O_4 \cdot 1.5H_2O$]				Raman	Birnessite is a slightly reduced phase, typical primary microbially mediated mineral.
Manjiroite [$Na(Mn^{4+}{}_7Mn^{3+})O_{16}$]				Raman	Manjiroite is a slightly reduced phase. Na-analogue.
Carbonates					
Rhodochrosite ($MnCO_3$)				Raman	Rhodochrosite is a typical early diagenetic product formed via suboxic heterotrophic microbially mediated processes (Polgári et al., 1991, and many other references), containing mineralized "organic carbon" in the carbonate. Mn^{2+} can originate from hydrothermal sources.
Oxides-silcates					
Braunite ($Mn^{2+}Mn^{3+}{}_6SiO_{12}$)				XRD, FTIR	Braunite probably is primary sedimentary or early diagenetic in origin. It may have grown by reaction between Mn^{2+}, liberated from older manganese oxides by the decay of trapped organic remains, or by infiltration of hydrothermal Mn^{2+} and silica (Serdyuchenko, 1980; Ostwald and Bolton, 1990). Biogeochemical formation has also been proposed (Rajabzadeh et al., 2017).
Fe mineral asssemblage					Hematite, goethite and also magnetite and maghemite can form through dehydration and transformation of certain iron oxyhydroxide minerals, such as lepidocrocite and ferrihydrite, which are typical microbially mediated minerals of Fe-oxidizing microbes (FeOB) (Ehrlich, 2002). The ferrihydrite stabilization is accompanied by silica segregation (Schwertmann and Cornell, 2007).
Oxides and hydroxides					
Fe_2O_3 (Amorphous)				XRD	
Ferryhydrite (FeOOH)				FTIR	
Lepidocrocite [$Fe^{3+}O(OH)$]				FTIR	
Hematite (Fe_2O_3)				XRD, Raman	Also, hematite is normally formed under oxidizing conditions as a weathering product of iron minerals (*e.g.* pyrite, magnetite). It can also form as primary product in many

(*continued on next page*)

Table 5 (*continued*)

					environments.
Goethite (FeOOH)		—		FTIR	Also, goethite is normally formed under oxidizing conditions as a weathering product of iron minerals (*e.g.* pyrite, magnetite). It can slso form as primary product in many environments.
Magnetite ($Fe^{2+}Fe^{3+}{}_2O_4$)		—		OM	Magnetite is the most reduced phase, also it forms via reduction of more oxygenic Fe-oxide phases in a sedimentary system under oxygen deficient diagenetic conditions, but only as the result of heterotrophic microbially mediated processes (Anthony et al., 1997). Magnetite pseudomorphs after pyrite.
Sulfides					
Pyrite (FeS_2)		—		OM	Goethite pseudomorphs after pyrite.
Phosphates					
Duphrènite $[Fe^{2+}Fe^{3+}{}_4(PO_4)_3(OH)_5•2(H_2O)]$	—	—		FTIR OM	Secondary mineral, but here the fine microtexture points to primary or early diagenetic formation.
Others					
Apatite $[(Ca_{10}(PO_4)_6(OH, F, Cl)_2]$	—	—		FTIR OM	Ca-phosphate – biomineral, apatite possibly results from organically-derived phosphate by microbial activity (biomats).
Feldspar (albite) ($NaAlSi_3O_8$)	—	—		Raman, FTIR	Tuff material, and also mineralized early diagenetic cell and EPS material, Na substitution (metasomatism), no luminescence
Chalcedony (cryptocrystalline)	—	—	—	XRD, FTIR, Raman	(i) hydrothermal source (ii) segregation via ferrihydrite transformation into more stable minerals (iii) biosilica
Quartz (SiO_2)	—	—	—	XRD, FTIR, Raman OM	Tuff material, and also mineralized early diagenetic cell and EPS material, segregated silica, no luminescence
Tourmaline $[(Na,Ca)(Mg,Li,Al,Fe^{2+},Fe^{3+})_3(Al,Mg)_6(BO_3)_3 Si_6O_{18}(OH,O,F)_4]$		—		FTIR OM	Typical product under neutral-slightly basic and oxic-suboxic conditions. It can form by microbially mediated Fe oxide + silica, and organic matter contribution.
Whewellite $[Ca(C_2O_4)\ H_2O]$	—	—		FTIR OM	organic mineral
Beryllonite ($NaBePO_4$)	—			FTIR	Beryllium has a microbial connection. The similar behaviour of BeF_3*H_2O to phosphate can positively or negatively affect the numerous enzymatic and regulating phosphatase functions.
Berthierite ($FeSb_2S_4$)	—			FTIR	Sb (antimony) influence enzyme activity of microbial growth (E. coli, B. subtilis and S. aureus) (An and Kim, 2009). The T. ferrooxidans directly oxidize Sb2S3 mobilizing Sb in Fe-Mn-Cr rich environment (Wong et al- 1982).
Johannite $[Cu(UO_2)_2(SO_4)_2(OH)_2•8(H_2O)]$	—	—		Raman	Formed from the oxidation of uraninite (UO_2), usually in the presence of gypsum. Occurs in granitic and syenitic pegmatites, colloform crusts in high-temperature hydrothermal veins, in quartz-pebble conglomerates.
Organic material	—			FTIR, Raman	

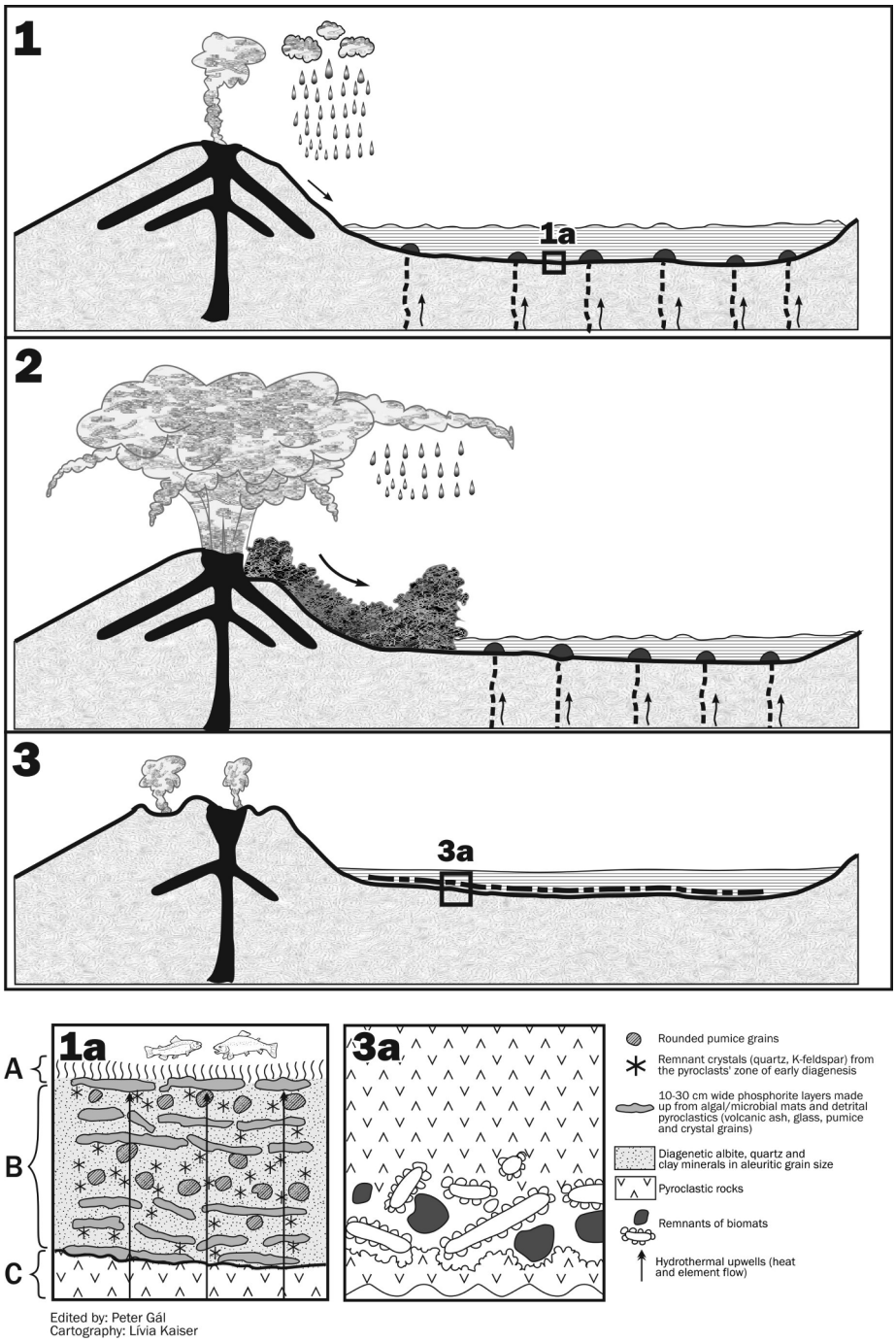

Fig. 15. Model of main steps of formation: (1) Shallow sea with volcanic islands and shallow basins between them represents the environment of accumulation. Phosphorite and siliceous bodies form due to hydrothermal solutions and microbial activity; (2) An explosive eruption generates dense pyroclastic flows, which reach the basin; (3) After the main stage of eruptions, thick pyroclastic layers cover the fragmented layers of the phosphorite and the blocks of the siliceous bodies, terminating the formation of phosphorite. Legend on 1a: A - The recent, still living and dead algal/microbial mats adsorb P, Mn, U, Be, REE, chalcophile elements from hydrothermal upwells, microorganisms build up phosphorous to rock forming quantity; B - Zone of early diagenesis: the decomposing algal/microbial mats fossilise by forming apatite-rich layers, the glassy material of pyroclasts crystallizes into quartz, feldspar, clay minerals, etc., which form silicate-rich layers; C - Pyroclastic rocks in basement.

directly oxidize Sb_2S_3 mobilizing Sb in Fe-Mn-Cr rich environment (Wong et al., 1982).

The V is bioessential element, controlls the sodium pumbp and inhibition ATPase, p-transferases (Frieden, 1985). Inside the cell, V (IV) is actively involved in phytoplankton metabolism. $NO_3-/NH_4^{\pm}$, Fe^{3+}/Fe^{2+}, MnO_2/Mn^{2+}, and SO_4^{2-}/H_2S may potentially play an important role in V speciation and cycling in the water column. (V) is stable in oxidized marine environments, while V (IV) is stable in moderately reducing environments, dissolved V occur in coastal waters within suboxic condition (Wang and Wilhelmy, 2009). The element enrichment of the Bükkszentkereszt occurrence (U, Be, P, Mn, Fe) and the positive correlation of U-P, Be-P and REE-P (Szabó and Vincze, 2013) reflect the features of microbial processes and can be interpreted as the result of those processes.

5.6. Genetic model

The main steps of formation are summarized in Fig. 15 as follows:

1. Permian-Lower Triassic shallow sea with volcanic islands and shallow basins (between them they represented the environment of accumulation). Rhyolitic volcanism occurred together with hydrothermal discharge systems in the basin floor (transporting heat and dissolved elements), circulating in the footwall volcanic rock sequence and forming massive siliceous bodies. Intense microbial mediation formed biomats on the surface in the basin, which concentrated Mn, U, Be, REE, and chalcophile elements from hydrothermal fluids. The substrate could be an earlier pyroclastic flow deposit. Though Fe is not enriched in the system, it also had a basic role as Fe-oxidizing microbes (FeOB) mineralized ferrihydrite, which offered an oxic catalytic surface

for Mn enrichment under suboxic semi-neutral conditions (Morgan, 2005; Polgári et al., 2012b). Higher oxygen supply supported enzymatic Mn oxidation (Villalobos et al., 2003; Morgan, 2005). Fe- and Mn-oxides adsorbed high quantities of P, U, Be, REE and some chalcophile elements (As, Cd, Cu, Pb, S, Sb, Se, Sn, Zn). Remnants of Fe-biomats support this scenario. Mn oxidizing bacteria selectively enriched REE via enzymatic processes (Moffett and Ho, 1996). A similar case resulted in the elevated Ce content in the Jurassic Úrkút Mn deposit in Hungary (Polgári et al., 2012b). Beryllium enrichment most probably occurred via organic matter binding, similarly to coal-bearing enrichments (Eskenazy, 1987). The microbial activity was randomly stopped by coarser and/or finer volcanic ash contribution, also by weathered pyroclastic fragments transported from the surface of volcanoes washed into the sea. Rounded pumice grains are embedded and porphyric crystals from pyroclastic material (quartz, K-feldspar). Microbes quickly re-colonized the tuff material. The separation of older biomats from water mass by tuff restricted re-utilization of P and resulted in its enrichment in the form of Ca phosphate (apatite) in rock forming quantity.

The zone of early diagenesis just below the sediment surface was characterized by embedded organic matter (cells and EPS), which influenced mineralization via fluffy spherical and ribbon-like apatite layers (mineralized biomats). Alteration of pyroclastic material also occurred: glassy material turned to quartz, feldspar, or clay minerals, which formed silicate-rich layers. Intense apatitization of tuff material took place (apatitized pumice grains). After the death of cells, the decomposition of cells and EPS started and ions bound on their surface were released. A complex transforming mineralization started, which resulted in clay mineral formation, mixed carbonates, feldspar (albitization), beryllonite, quartz, apatite, etc., depending on the geochemical conditions. These poorly crystalline minerals formed more stable minerals over time (Konhauser, 1998; Dupraz and Visscher, 2005). Quartz and feldspar grains of the debris-like layers do not show luminescence, which supports their authigenic origin.

2. An explosive eruption generated dense pyroclastic flows and a basal avalanche occurred in the lowest part of the pyroclastic flow, in which increased particle concentration developed due to gravity segregation. This avalanche caused substrate erosion, or after lithification of the pyroclastic flow, the load processes caused deformation of the substrate.

3. After the main stage of eruptions, thick pyroclastic (ignimbrite) layers covered the fragmented layers of the phosphorite and the blocks of the siliceous bodies. The cause of fragmentation is still not confirmed: (i) either the basal avalanche tore open the phosphorite layers or (ii) the layers were torn apart by later load processes due to the different properties in hardness of the pyroclastic rocks and phosphorite layers.

In the lowest portion of the younger pyroclastic layer fragmented pieces of phosphorite occur, where the edge of the lens-like phosphorite pieces often has a micro-brecciated edge. Small clasts of the hydrothermal silica bodies are incorporated. The siliceous rock remained only as small pieces in the breccia of the excavated phosphorite occurrences (Shaft-II, Excavation No. 40).

4. The Permian-Lower Triassic rock series was covered by Upper Triassic limestones and Jurassic turbidite sediments of at least 6–14 km thickness. Cretaceous low-grade Alpine metamorphism caused an increase in pressure (2.5–3 kbar) and temperature (T_{max}: 350 °C) and the formation of a huge quantity of sericite within the metamorphic series.

Strongly folded schistose meta-volcanic layers contain the lensoid phosphorite bodies, which more recently formed pieces of fragmented layers of the phosphorite and the siliceous rock, which alternate in 2–3 m thickness. New deformation processes also caused brecciation, while strong folding and shearing effects are also common. Deformed phosphorite bodies form lenses of 30–50 m size after the original layers suffered shear deformation and were broken into pieces by faults.

5. The area was uplifted and erosion took place, which resulted in the occurrence of phosphorite lenses near the surface and at shallow depths, and the occurrences are strongly fractured by tectonics.

6. Conclusion

A multiphase formation model was elaborated based on a complex dataset made up of recent and earlier published results on the geology, petrology, macro- and micro-texture, bulk and *in situ* mineralogy, and also the distribution of embedded organic matter and geochemical features (main and trace elements, REE) of strongly deformed phosphorite layers enriched in U-Be-Mn-REE occurring in weathered Triassic metarhyolite tuff in NE Hungary. The genetic draft supports post-volcanic exhalative-hydrothermal activity as the element source.

Based on the element enrichments, the micro-textural features and the mineralogical composition, a further enrichment effect is proposed in addition to the hydrothermal origin (source). In the case of P, Mn, Fe, U, As, Zn, and also the REEs, the effect of microbial mediation can be raised. This scenario is supported by the correlation of elements and also the mineralogical composition among which bioindicator minerals occur, such as collophane, Mn-oxides, Fe-phosphate, Fe-oxide-hydroxide, pyrite and also the U-minerals.

Summarizing our results, the meta-rhyolite-hosted Mn-P-U-Be-REE mineralization bond U-Be-REE-phosphate enrichment at Bükkszentkereszt can be proposed as a fossil mineralized microbially mediated deposit.

Declaration of Competing Interest

The authors declare that they have no known competing financial interests or personal relationships that could have appeared to influence the work reported in this paper.

Acknowledgments

The authors thank for the support by the National Research, Development and Innovation Office, National Scientific Research Fund No. 125060, Support of Excellence of the Research Centre for Astronomy and Geosciences, Institute for Geological and Geochemical Research. Comments of anonymous reviewers are highly appreciated.

References

Abdelouas, A., Lu, Y.M., Lutze, W., Nuttall, H.E., 1998. Reduction of U(VI) to U(IV) by indigenous bacteria in contaminated ground water. J. Contam. Hydr. 35 (1–3), 217–233. https://doi.org/10.1016/S0169-7722(98)00134-X.

Abed, A.M., Fakhouri, K., 1990. Role of microbial processes in the genesis of Jordanian Upper Cretaceous phosphorites. Geol. Soc. Lond. Spec. Publ. 52 (1), 193–203. https://doi.org/10.1144/GSL.SP.1990.052.01.14.

An, Y.J., Kim, M., 2009. Effect of antimony on the microbial growth and the activities of soil enzymes. Chemosphere 74 (5), 654–659.

Árkai, P., 1983. Very low-and low-grade Alpine regional metamorphism of the Paleozoic and Mesozoic formations of the Bukkium. NE-Hungary. Acta Geol. Hung. 26 (1–2), 83–101.

Árkai, P., Balogh, K., Dunkl, I., 1995. Timing of low-temperature metamorphism and cooling of the Paleozoic and Mesozoic formations of the Bükkium, innermost Western Carpathians. Hungary. Geol. Rundsch. 84 (2), 334–344.

Bailey, J.V., Corsetti, F.A., Greene, S.E., Crosby, C.H., Liu, P., Orphan, V.J., 2013. Filamentous sulfur bacteria preserved in modern and ancient phosphatic sediments: implications for the role of oxygen and bacteria in phosphogenesis. Geobiology 11 (5), 397–405. https://doi.org/10.1111/gbi.12046.

Bárdossy, G., Bottyán, L., Gadó, P., Griger, Á., Sasvári, J., 1980. Automated quantitative phase analysis of bauxites. Am. Min. 65 (1–2), 135–141.

Beasley, M.M., Bartelink, E.J., Taylor, L., Miller, R.M., 2014. Comparison of transmission FTIR, ATR, and DRIFT spectra: implications for assessment of bone bioapatite diagenesis. J. Archaeol. Sci. 46, 16–22. https://doi.org/10.1016/j.jas.2014.03.008.

Berthelin, J., Munier-Lamy, C., 1983. Microbial mobilization and preconcentration of uranium from various rock materials by fungi. Ecol. Bull. 395–401.

Billon, G., Ouddane, B., Proix, N., Desormieres, J., Abdelnour, Y., Boughriet, A., 2004. The chemical behavior of sedimentary uranium in Authie Bay (France). Int. J. Envir. Anal. Chem. 84 (10), 775–787. https://doi.org/10.1080/03067310410001729079.

Biondi, J.C., Polgári, M., Gyollai, I., Fintor, K., Kovács, I., Fekete, J., Mojzsis, S.J., 2020. Biogenesis of the Neoproterozoic kremydilite manganese ores from Urucum (Brazil) –

a new manganese ore type. Precambrian Research 340, 105624. https://doi.org/10.1016/j.precamres.2020.105624.
Brooks, S.C., Fredrickson, J.K., Carroll, S.L., Kennedy, D.W., Zachara, J.M., Plymale, A.E., Kelly, S.D., Kemner, K.M., Fendorf, S., 2003. Inhibition of bacterial U(VI) reduction by calcium. Envir. Sci. & Techn. 37 (9), 1850–1858. https://pubs.acs.org/doi/abs/10.1021/es0210042.
Chen, K., Leona, M., Vo-Dinh, T., 2007. Surface-enhanced Raman scattering for identification of organic pigments and dyes in works of art and cultural heritage material. SeRv 27, 109–120. https://doi.org/10.1108/02602280710731678.
Cook, P.J., McElhinny, M.W., 1979. A reevaluation of the spatial and temporal distribution of sedimentary phosphate deposits in the light of plate tectonics. Econ. Geol. 74 (2), 315–330. https://doi.org/10.2113/gsecongeo.74.2.315.
Crosby, C.H., Bailey, J., 2012. The role of microbes in the formation of modern and ancient phosphatic mineral deposits. Frontiers in microbiology 3, 241.
Csáki, F., Csáki, F.-né, 1973. Summary report on the prospecting at the Bükkszentkereszt area between 1969 and 1973. MÉV manuscript, Mecsekérc Inc., Data bank. In Hungarian.
Das, S., Hendry, M.J., 2014. Characterization of hematite nanoparticles synthesized via two different pathways. J. Nanoparticle Res. 16 (8), 2535. https://doi.org/10.1007/s11051-014-2535-7.
Dill, H.G., 2010. The "chessboard" classification scheme of mineral deposits: Mineralogy and geology from aluminum to zirconium. Earth Science Reviews 100, 1–420.
Dupraz, C., Visscher, P.T., 2005. Microbial lithification in marine stromatolites and hypersaline mats. Trends Microbiol. 13 (9), 429–438. https://doi.org/10.1016/j.tim.2005.07.008.
Dwivedy, K.K., Mathur, A.K., 1995. Bioleaching - our experience. Hydrometallurgy 38 (1), 99–109. https://doi.org/10.1016/0304-386X(94)00034-Z.
Ehrlich, H.L., 2002. How microbes mobilize metals in ores: A review of current understandings and proposals for further research. Mining, Metal. & Expl. 19 (4), 220–224. https://doi.org/10.1007/BF03403273.
Elias, D.A., Senko, J.M., Krumholz, L.R., 2003. A procedure for quantitation of total oxidized uranium for bioremediation studies. J. Microbiol. Methods 53 (3), 343–353. https://doi.org/10.1016/S0167-7012(02)00252-X.
Eskenazy, G.M., 1987. Rare earth elements in a sampled coal from the Pirin deposit. Bulgaria. Int. J. Coal Geol. 7 (3), 301–314. https://doi.org/10.1016/0166-5162(87)90041-3.
Filipović, I., Jovanović, D., Sudar, M., Pelikán, P., Kovács, S., Less, G., Hips, K., 2003. Comparison of the Variscan-Early Alpine evolution of the Jadar Block (NW Serbia) and Bükkium (NE Hungary) terranes; some paleogeographic implications. Slovak Geol. Mag. 9 (1), 23–40.
Fortin, D., Ferris, F.G., Beveridge, T.J., 1997. Surface-mediated mineral development by bacteria. Miner. Soc. Am. Revs Min. 35, 161–180.
Fowle, D.A., Fein, J.B., Martin, A.M., 2000. Experimental study of uranyl adsorption onto Bacillus subtilis. Envir. Sci. & Techn. 34 (17), 3737–3741. https://doi.org/10.1021/es991356h.
Francis, A.J., Gillow, J.B., Dodge, C.J., Harris, R., Beveridge, T.J., Papenguth, H.W., 2004. Uranium association with halophilic and non-halophilic bacteria and archaea. Radiochim. Acta 92 (8), 481–488. https://doi.org/10.1524/ract.92.8.481.39281.
Fredrickson, J.K., Zachara, J.M., Kennedy, D.W., Liu, C.X., Duff, M.C., Hunter, D.B., Dohnalkova, A., 2002. Influence of Mn oxides on the reduction of Uranium(VI) by the metal-reducing bacterium Shewanella putrefaciens. Geochim. Cosmochim. Acta 66 (18), 3247–3262. https://doi.org/10.1016/S0016-7037(02)00928-6.
Frieden, E., 1985. New perspectives on the essential trace elements. APS Publications.
Frost, R.L., Erickson, K.L., Čejka, J., Reddy, B.J., 2005. A Raman spectroscopic study of the uranyl sulphate mineral johannite. Spectrochim. Acta Part A: Mol. Biomol. Spectr. 61 (11–12), 2702–2707. https://doi.org/10.1016/j.saa.2004.10.013.
Frost, R.L., Xi, Y., Scholz, R., López, A., Belotti, F.M., 2013. Vibrational spectroscopic characterization of the phosphate mineral hureaulite–(Mn, Fe)$_5$(PO$_4$)$_2$(HPO$_4$)$_2$·4(H$_2$O). Vibr. Spectr. 66, 69–75. https://doi.org/10.1016/j.vibspec.2013.02.003.
Gál, P., Lukács, R., Józsa, S., Dunkl, I., Németh, N., Harangi, S., 2018. Results of the petrographical, geochemical and geochronological reinvestigation of the Triassic metavolcanic rocks at Bükkszentlászló, Bükk Mts. Geological Association, Salzburg.
Glotch, T.D., Rossman, G.R., 2009. Mid-infrared reflectance spectra and optical constants of six iron oxide/oxyhydroxide phases. Icarus 204 (2), 663–671. https://doi.org/10.1016/j.icarus.2009.07.024.
Gyollai, I., Polgári, M., Fintor, K., Pál-Molnár, E., Popp, F., Koeberl, C., 2017. Microbial activity records in Marinoan Snowball Earth postglacial transition layers connecting diamictite with cap carbonate (Otavi Group, NW-Namibia). Austrian J. Earth Sci. 110 (1), 2–18. https://doi.org/10.17738/ajes.2017.0001.
Gyollai, I., Polgári, M., Veres, M., Nagy, S., Popp, F., Mader, D., Koeberl, C., 2014. Evidence of microbial activity involved with Neoproterozoic postglacial sediments from the Otavi Group, Namibia: a study of Sturtian oolitic carbonate sandstone with spectroscopic methods. Comm. Nam. Geol. Surv. 117–133.
Gyollai, I., Polgári, M.P., Fintor, K., Popp, F., Mader, D., Pál-Molnár, E., 2015. Microbially mediated deposition of postglacial transition layers from the Neoproterozoic Otavi Group, Namibia: evidence of rapid deglaciation after the Sturtian cryogenic period. Carpathian J. Earth & Envir. Sci. 10 (1), 63–76.
Haas, J., Budai, T., Csontos, L., Fodor, L., Konrád, G., Koroknai, B., 2014. Geology of the pre-Cenozoic basement of Hungary. Geological and Geophysical Institute of Hungary, Budapest, pp. 1–71.
Henry, D.J., Dutrow, B.L., 2012. Tourmaline at diagenetic to low-grade metamorphic conditions: Its petrologic applicability. Lithos 154, 16–32. https://doi.org/10.1016/j.lithos.2012.08.013.
Jarvis, I., 1995. Phosphorite geochemistry: state-of-the-art and environmental concerns. Ecl. Geol. Helv. 87 (3), 656–664.
Jehlička, J., Edwards, H.G.M., Vítek, P., 2009. Assessment of Raman spectroscopy as a tool for the non-destructive identification of organic minerals and biomolecules for Mars studies. Planet. Space Sci. 57, 606–613. https://doi.org/10.1016/j.pss.2008.05.005.
Julien, C.M., Massot, M., Poinsignon, C., 2004. Lattice vibrations of manganese oxides: Part I. Periodic structures. Spectrochim. Acta Part A: Mol. & Biomol. Spectr. 60 (3), 689–700. https://doi.org/10.1016/S1386-1425(03)00279-8.
Kalinowski, B.E., Oskarsson, A., Albinsson, Y., Arlinger, J., Odegaard-Jensen, A., Andlid, T., Pedersen, K., 2004. Microbial leaching of uranium and other trace elements from shale mine tailings at Ranstad. Geoderma 122 (2–4), 177–194. https://doi.org/10.1016/j.geoderma.2004.01.007.
Khijniak, T.V., Slobodkin, A.I., Coker, V., Renshaw, J.C., Livens, F.R., Bonch-Osmolovskaya, E.A., Birkeland, N.K., Medvedeva-Lyalikova, N.N., Lloyd, J.R., 2005. Reduction of uranium(VI) phosphate during growth of the thermophilic bacterium Thermoterrabacterium ferrireducens. Appl. & Env. Microbiol. 71 (10), 6423–6426. https://doi.org/10.1128/AEM.71.10.6423-6426.2005.
Knoll, A.H., Canfield, D.E., Konhauser, K.O., 2012. Fundamentals of Geobiology. Wiley-Blackwell, Oxford, pp. 456.
Knopp, R., Panak, P.I., Wray, L.A., Renninger, N.S., Keasling, J.D., Nitsche, H., 2003. Laser spectroscopic studies of interactions of U-VI with bacterial phosphate species. Chemistry-A Eur. J. 9 (12), 2812–2818. https://doi.org/10.1002/chem.200304711.
Kolodny, Y., Luz, B., 1992. Isotope signatures in phosphate deposits: Formation and diagenetic history. In: Isotopic Signatures and Sedimentary Records. Springer, Berlin, Heidelberg, pp. 69–121.
Konhauser, K.O., 1998. Diversity of bacterial iron mineralization. Earth-Sci. Rev. 43 (3–4), 91–121. https://doi.org/10.1016/S0012-8252(97)00036-6.
Kovács, S., Haas, J., 2010. Displaced South Alpine and Dinaridic elements in the mid-Hungarian zone. Central Eur. Geol. 53 (2–3), 135–164. https://doi.org/10.1556/CEuGeol.53.2010.2-3.3.
Kubovics, I., Nagy, B., Nagy-Balogh, J., Puskás, Z., 1989. Beryllium and some other rare element contents of acid volcanics (tuffs) and metamorphites in Hungary. —. Acta Geologica Hungarica 21 (1–2), 219–231.
Lafuente, B., Downs, R.T., Yang, H., Stone, N., 2015. In: RRUFF Database (Database of Raman spectroscopy, X-ray diffraction, and chemistry of minerals, pp. 1–30.
Lamboy, M., 1990. Microbial mediation in phosphatogenesis: new data from the Cretaceous phosphatic chalks of northern France. Geol. Soc. Lond. Spec. Publ. 52 (1), 157–167. https://doi.org/10.1144/GSL.SP.1990.052.01.11.
Landa, E.R., 2003. Mobilization of radionuclides from uranium mill tailings and related waste materials in anaerobic environments. J. Radioanal. Nucl. Chem. 255 (3), 559–563. https://doi.org/10.1023/A:1022501003604.
Less G., Kovács, S., Pelikán, P., Pentelényi, L. & Sásdi, L., 2005. Geology of the Bükk Mountains. Explanatory book to the geological map of the Bükk Mountains (1:50000) Geological Institute of Hungary, Budapest, 2005, pp. 284 (in Hungarian).
Levinson, A.A., 1962. Beryllium-fluorine mineralization at Aguachile. Mountain, Coahuila, Mexico. Am. Min.: J. Earth & Planet. Mater. 47 (1–2), 67–74.
Lindsey, D.A., 1977. Epithermal beryllium deposits in waterlaid tuff, western Utah. Econ. Geol. 72, 219–232. https://doi.org/10.2113/gsecongeo.72.2.219.
Lovley, D.R., 1991. Dissimilatory Fe (III) and Mn (IV) reduction. Microbiology and Molecular Biology Reviews 55 (2), 259–287.
Lovly, D.R., 1993. Dissimilatory metal reduction. Ann. Rev. Microbiol. 47, 263–290. https://doi.org/10.1146/annurev.mi.47.100193.001403.
Lovly, D.R., Roden, E.E., Phillips, E.J.P., Woodward, J.C., 1993. Enzymatic iron and uranium reduction by sulfate-reducing bacteria. Mar. Geol. 113 (1–2), 41–53. https://doi.org/10.1016/0025-3227(93)90148-O.
Macaskie, L.E., Empson, R.M., Lin, F., Tolley, M.R., 1995. Enzymatically-mediated uranium accumulation and uranium recovery using a Citrobacter sp immobilized as a biofilm within a plug-flow reactor. J. Chem. Techn. & Biotechn. 63 (1), 1–16. https://doi.org/10.1002/jctb.280630102.
Madejová, J., Komadel, P., 2001. Baseline studies of the clay minerals society source clays: infrared methods. Clays & Clay Min. 49, 410–432.
Marquis, R.E., Clock, S.A., Mota-Meira, M., 2003. Fluoride and organic weak acids as modulators of microbial physiology. FEMS Microbiol. Revs 26 (5), 493–510. https://doi.org/10.1111/j.1574-6976.2003.tb00627.x.
Marshall, D.J., 1998. Cathodoluminescence of Geological Materials. Unwin Hyman, Boston, pp. 146.
Moffett, J.W., Ho, J., 1996. Oxidation of cobalt and manganese in seawater via a common microbially catalyzed pathway. Geochim. Cosmochim. Acta 60 (18), 3415–3424.
Moffett, J.W., 1994. The relationship between cerium and manganese oxidation in the marine-environment. Limnology and Oceanography 39 (6), 1309–1318.
Moffett, J.W., 1990. Microbially meddiated cerium oxidation in sea-water. Nature 345 (6274), 421–423.
Morgan, J.J., 2005. Kinetics of reaction between O2 and Mn(II) species in aqueous solutions. Geochim. Cosmochim. Acta 69 (1), 35–48. https://doi.org/10.1016/j.gca.2004.06.013.
Müller, C.M., Pejcic, B., Esteban, L., Delle Piane, C., Raven, M., Mizaikoff, B., 2014. Infrared attenuated total reflectance spectroscopy: an innovative strategy for analyzing mineral components in energy relevant systems. Sci. Reps 4, 6764. https://doi.org/10.1038/srep06764.
Nagy, B., 2006. K-rich rocks and their relation to mineralization in the Mátra Mountains (North Hungary). Acta Geol. Hungarica, Central Eur. Geol. 49 (1), 33–41.
Németh, N., Pethő, G., Zajzon, N., 2015. In situ gamma ray survey for geological mapping of K-metasomatized metavolcanics at Bükkszentkereszt, Bükk Mts, Hungary. Open. Geosciences 7 (1). https://doi.org/10.1515/geo-2015-0033.
Okolo, G.N., Neomagus, H.W., Everson, R.C., Roberts, M.J., Bunt, J.R., Sakurovs, R., Mathews, J.P., 2015. Chemical–structural properties of South African bituminous coals: Insights from wide angle XRD–carbon fraction analysis, ATR–FTIR, solid state 13C NMR, and HRTEM techniques. Fuel 158, 779–792. https://doi.org/10.1016/j.

fuel.2015.06.027.
Orange, D., Knittle, E., Farber, D., Williams, Q., 1996. Raman spectroscopy of crude oilsand hydrocarbon fluid inclusions: A feasibility study. Geochem. Soc. Spec. Publ. 5, 65–81.
Ostwald, J., Bolton, B.R., 1990. Diagenetic braunite in sedimentary rocks of the Proterozoic Manganese Group. Western Australia. Ore Geol. Revs 5 (4), 315–323. https://doi.org/10.1016/0169-1368(90)90036-M.
Panak, P.J., Knopp, R., Booth, C.H., Nitsche, H., 2002. Spectroscopic studies on the interaction of U(VI) with Bacillus sphaericus. Radiochim. Acta 90 (9–11), 779–783. https://doi.org/10.1524/ract.2002.90.9-11_2002.779.
Parikh, S.J., Chorover, J., 2006. ATR-FTIR spectroscopy reveals bond formation during bacterial adhesion to iron oxide. Langmuir 22 (20), 8492–8500. https://doi.org/10.1021/la061359p.
Park, J., Jeters, R.T., Kuo, L.J., Strivens, J.E., Gill, G.A., Schlafer, N.J., Bonheyo, G.T., 2016. Potential impact of seawater uranium extraction on marine life. Industrial & Engineering Chemistry Research 55 (15), 4278–4284.
Peśic, L., Ramović, A., Sremac, J., Pantić-Prodanović, S., Filipović, I., Kovács, S., Pelikán, P., 1988. Upper Permian deposits of the Jadar region and their position within the Western Paleotethys. Memorie della Societa Geologica Italiana 34, 211–219.
Polgári, M., 2016. A possible alternative genetic interpretation of Mn-P-U-Be-REE mineralization, Bükkszentkeret, Bükk Mts, Hungary, V. Terrestrial Radioisotopes in environment. International Conference on Environmental Protection (2016) Veszprém. p. 80.
Polgári, M., Gál, P., Józsa, S., Gyollai, I. & Fintor, K., 2018. Contribution to the origin of the P-Mn-U-Be-HREE-enrichment in phosphatite, near Bükkszentkereszt, NE Hungary. VI. Terrestrial Radioisotopes in Environment: International Conference on Environmental Protection. p. 31.
Polgári, M., Gyollai, I., Fintor, K., Horváth, H., Pál-Molnár, E., Biondi, J.C., 2019. Microbially mediated ore forming processes and the cell mineralization. Front. Microbiol. 10, 2731. https://doi.org/10.3389/fmicb.2019.02731.
Polgári, M., Hein, J.R., Tóth, A.L., Pál-Molnár, E., Vigh, T., Bíró, L., Fintor, K., 2012a. Microbial action formed Jurassic Mn-carbonate ore deposit in only a few hundred years (Úrkút, Hungary). Geology 40 (10), 903–906. https://doi.org/10.1130/G33304.1.
Polgári, M., Hein, J.R., Vigh, T., Szabó-Drubina, M., Fórizs, I., Bíró, L., Müller, A., Tóth, A.L., 2012b. Microbial processes and the origin of the Úrkút manganese deposit. Hungary. Ore Geol. Revs 47, 87–109. https://doi.org/10.1016/j.oregeorev.2011.10.001.
Polgári, M., Okita, P.M., Hein, J.R., 1991. Stable isotope evidence for the origin of the Úrkút manganese ore deposit. Hungary. J. Sed. Pet. 61 (3), 384–393. https://doi.org/10.1306/D426771C-2B26-11D7-8648000102C1865D.
Polgári, M., Szabó, Z. & Szederkényi, T. (Eds.), 2000. Manganese Ores in Hungary – In Commemoration of Professor Gyula Grasselly – Hungarian Academy of Sciences. Juhász Publishing House, Szeged. pp. 675.
Pracejus, B., Bolton, B.R., Frakes, L.A., 1988. Nature and development of supergene manganese deposits, Groote Eylandt, Northern Territory, Australia. Ore Geology Reviews 4 (1/2), 71–99.
Pufahl, P.K., Groat, L.A., 2017. Sedimentary and igneous phosphate deposits: formation and exploration: an invited paper. Econ. Geol. 112 (3), 483–516. https://doi.org/10.2113/econgeo.112.3.483.
Rajabzadeh, M.A., Haddad, F., Polgári, M., Fintor, K., Walter, H., Molnár, Z., Gyollai, I., 2017. Investigation on the role of microorganisms in manganese mineralization from Abadeh-Tashk area, Fars Province, southwestern Iran by using petrographic and geochemical data. Ore Geol. Revs 80, 229–249. https://doi.org/10.1016/j.oregeorev.2016.06.035.
Robles, L.C., Aller, A.J., 1994. Preconcentration of beryllium on the outer-membrane of escherichia-coli and pseudomonas-putida prior to determination by electrothermal atomic-absorption spectrometry. J. Anal. Atomic Spectr. 9(8), 871-879. doi: 10.1039/JA9940900871.
Schippers, A., Hallmann, R., Wentzien, S., Sand, W., 1995. Microbial diversity in uranium-mine waste heaps. Appl. Environ. Microbiol. 61 (8), 2930–2935.
Schwertmann, U. & Cornell, R.M., 2007. Iron Oxides in the Laboratory: Preparation and Characterization. Wiley-VCH, pp. 188.
Selmeczi, B.-né, Antal, P., 1974. Analytical data of Bükkszentkereszt research area (summary report, Mecsek Ore Exploration Ltd., Kővágószőlős) (in Hungarian), pp. 48–49.
Sepúlveda, M., Gutiérrez, S., Vallette, M.C., Standen, V.G., Arriaza, B.T., Cárcamo-Vega, J.J., 2015. Micro-Raman spectral identification of manganese oxides black pigments in an archaeological context in Northern Chile. Herit. Sci. 3 (1), 32. https://doi.org/10.1186/s40494-015-0061-2.
Skinner, H.C.W., 1993. A review of apatites, iron and manganese minerals and their roles as indicators of biological-activity in black shales. Precambr. Res. 61 (3–4), 209–229. https://doi.org/10.1016/0301-9268(93)90114-H.
Southam, G., Sanders, J.A., 2005. The geomicrobiology of ore deposite. Econ. Geol. 100 (6), 1067–1084. https://doi.org/10.2113/gsecongeo.100.6.1067.
Stadnichenko, O.T., Zubovic, P., Sheffey, N.B., 1961. Beryllium content of American coals. Geol Surv. Bull. 1084-K, USA.
Suzuki, Y., Banfield, J.F., 2004. Resistance to, and accumulation of, uranium by bacteria from a uranium-contaminated site. Geomicrobiol. J. 21 (2), 113–121. https://doi.org/10.1080/01490450490266361.
Szabó, I., Vincze, J., 2013. U-Be-bearing and Mn-ore associated posphate mineralization of the rhyolite (quartzporphyry)-tuff, at Bükkszentkereszt (NE Hungary). Bull. Hung. Geol. Surv. 143 (1), 3–29. http://doi10.1515/geo-2015-0033.
Szoldán, A., 1990. Middle Triassic magmatic sequences from different tectonic settings in the Bükk Mts. (NE Hungary). Acta Mineralogica-Petrographica 31, 25–42.
Tebo, B.M., Obraztsova, A.Y., 1998. Sulfate-reducing bacterium grows with Cr(VI), U(VI), Mn(IV), and Fe(III) as electron acceptors. FEMS Microbiol. Letts 162 (1), 193–198. https://doi.org/10.1111/j.1574-6968.1998.tb12998.x.
Texier, A.C., Andres, Y., Illemassene, M., Le Cloirec, P., 2000. Characterization of lanthanide ions binding sites in the cell wall of Pseudomonas aeruginosa. Envir. Sci. & Techn. 34 (4), 610–615. https://doi.org/10.1021/es990668h.
Vaidya, R.U., Brozik, S.M., Deshpande, A., Hersman, L.E., Butt, D.P., 1999. Protection of beryllium metal against microbial influenced corrosion using silane self-assembled monolayers. Metal. & Mat. Transact. A – Phys. Metall. & Mat. Sci. 30 (8), 2129–2134. https://doi.org/10.1007/s11661-999-0024-x.
Varga, Gy, 1992. K metasomatized andezite from Mátra Mountains. Annual Report of Hungarian Geological Survey from 1990, 241–276 (in Hungarian).
Varnavas, S.P., Papavasiliou, C., 2020. Submarine hydrothermal mineralization processes and insular mineralization in the Hellenic Volcanic Arc system: A Review. Ore Geology Reviews 103541.
Villalobos, M., Toner, B., Bargar, J., Sposito, G., 2003. Characterization of the manganese oxide produced by Pseudomonas putida strain MnB1. Geochim. Cosmochim. Acta 67 (14), 2649–2662. https://doi.org/10.1016/S0016-7037(03)00217-5.
Wackett, L., Dodge, A.G., Ellis, L.B.M., 2004. Microbial genomics and the Periodic Table. Applied and Environmental Microbiology. 70 (2), 647–655. https://doi.org/10.1128/AEM.70.2.647-655.2004.
Wang, D., Wilhelmy, S.A.S., 2009. Vanadium speciation and cycling in coastal waters. Marine Chemistry 117 (1–4), 52–58.
Wong, C., Silver, M., Kushner, D.J., 1982. Effects of chromium and manganese on Thiobacillus ferrooxidans. Canadian Journal of Microbiology 28 (5), 536–544.
Yu, W., Polgári, M., Gyollai, I., Fintor, K., Szabó, M., Kovács, I., Fekete, J., Du, Y., Zhou, Q., 2019. Microbial metallogenesis of Cryogenian manganese ore deposits in South China. Precambr. Res. 322, 122–135. https://doi.org/10.1016/j.precamres.2019.01.004.
Zajzon, N., Németh, N., Szakáll, S., Gál, P., Kristály, F., Móricz, F., Fehér, B., 2014. REE in the Mn-U-Be geochemical anomaly at Bükkszentkereszt. In: Földessy, J. (Ed.), CriticEl Monography Series, 5. Millagrossa Ltd, Miskolc, pp. 92–108.